Metal nanoparticle collection and in-flight functionalization for circular femtosecond laser micromachining

by

Gianluca Zeppetelli

Department of Chemical Engineering

McGill University, Montreal

June 2024

Under the supervision of

Professors Anne-Marie Kietzig and Sylvain Coulombe

A thesis submitted to McGill University in partial fulfillment of the requirements of the degree of Master of Science in Chemical Engineering

Abstract

Femtosecond pulsed laser micromachining is an advanced machining technique where material is ablated from a surface to produce desired structures. This process generates nanoparticles, which in industrial settings become trapped in a high efficiency particulate air filter. Therefore, this project focused on recovering nanoparticles by collecting the ejected nanoparticles at the point of ablation. The goal was to optimize operating settings for a nanoparticle collector consisting of a rod-shaped electrode contained in a tube that is connected to a suction line. Tunable process parameters were the flowrate in the suction line and the laser machining stage velocity. For a fixed laser fluence of 4.5 times the ablation threshold, three suction flowrates (0, 0.57, and 1.13 m^3/h) and stage velocities (1, 5, and 10 mm/s) were considered to determine optimal collection parameters for an applied potential of 2.0 kV. Using copper as an initial target, the collection efficiency was determined by comparing the masses of collected and ablated material. We found that the highest stage velocity led to the best collection efficiency. This result is attributed to the increased distance between irradiated laser spots from subsequent pulses causing less interaction between an incoming pulse and the expanding nanoparticle plume from a previous pulse. Furthermore, the intermediate suction flowrate was optimal as it struck a balance between attracting the plume towards the electrode but not executing too much suction for the nanoparticles not to be collected. Using optimized collection settings, the effect of laser fluence was determined by running additional experiments at 3.0, 6.0, and 7.5 times the ablation threshold. Fluence dependent dynamics of ejected material affected the trajectory of nanoparticles towards the collector thus leading to disparities in collection efficiency. The effect of target material composition was investigated by comparing the collection of pure metals and alloys. Interestingly, depending on the elements present in the alloy, an enhancement in collection occurred. As an extension to the study on nanoparticle collection, a capacitively coupled dielectric barrier discharge plasma reactor was assembled to test a methodology for in-flight surface functionalization to produce organic layer coated metal nanoparticles. Due to the agglomeration of injected nanoparticles and fragmentation of the nanoparticles by the plasma, initial trials of the methodology were deemed unsuccessful. However, with further research, the implementation of such a system could be promising in the context of recovering material from laser ablation.

Résumé

Le micro-usinage au laser pulsé femtoseconde est une technique de fabrication avancée où le matériau est ablaté d'une surface pour produire des structures désirées. Ce processus génère des nanoparticules qui, dans des environnements industriels, sont piégées dans un filtre à haute efficacité. Par conséquent, ce projet vise à récupérer les nanoparticules en collectant celles éjectées au point d'ablation. L'objectif est d'optimiser les paramètres opérationnels pour un collecteur de nanoparticules composé d'une électrode en forme de tige contenue dans un tube connecté à une ligne d'aspiration. Les paramètres ajustables du procédé sont le débit dans la ligne d'aspiration et la vitesse de la platine de translation du laser. Pour une fluence laser fixe de 4,5 fois le seuil d'ablation, trois débits d'aspiration (0, 0,57 et 1,13 m^3/h) et trois vitesses de platine de translation (1, 5 et 10 mm/s) ont été considérés pour déterminer les paramètres de collecte optimaux pour une tension appliquée de 2,0 kV. En utilisant le cuivre comme matériau cible initial, l'efficacité de la collecte a été déterminée en comparant les masses de matériau collecté et ablaté. Nous avons constaté que la vitesse de platine de translation la plus élevée conduit à la meilleure efficacité de collecte. Ce résultat est attribué à l'augmentation de la distance entre les points laser irradiés par des impulsions successives, réduisant ainsi l'interaction entre une impulsion entrante et le panache de nanoparticules en expansion d'une impulsion précédente. De plus, le débit d'aspiration intermédiaire était optimal car il équilibrait l'attraction de la plume vers l'électrode sans exercer une aspiration excessive qui aurait empêché la collecte des nanoparticules. En utilisant les paramètres de collecte optimisés, l'effet de la fluence laser a été déterminé en menant des expériences supplémentaires à des fluences de 3,0, 6,0 et 7,5 fois le seuil d'ablation. Les dynamiques dépendantes de la fluence du matériau éjecté affectent la trajectoire des nanoparticules vers le collecteur, entraînant ainsi des disparités dans l'efficacité de collecte. L'effet de la composition du matériau cible a été étudié en comparant la collecte de métaux purs et d'alliages. De manière intéressante, selon les éléments présents dans l'alliage, une amélioration de la collecte a pu se produire. En prolongement du travail sur la collecte de nanoparticules, un réacteur plasma à décharge à barrière diélectrique couplée capacitivement a été assemblé pour tester une méthodologie de fonctionnalisation de surface en vol afin de produire des nanoparticules métalliques revêtues de couches organiques. En raison de l'agglomération des nanoparticules injectées et de la fragmentation des nanoparticules par le plasma, les premiers essais de la méthodologie ont été jugés infructueux. Cependant, avec des recherches supplémentaires, la mise

en œuvre d'un tel système pourrait être prometteuse dans le contexte de la récupération de matériau à partir de l'ablation laser.

Acknowledgements

It is my pleasure to give my most sincere acknowledgements to all the people who helped make this work possible. First and foremost, I would like to thank my research supervisors, Profs. Anne-Marie Kietzig and Sylvain Coulombe. Thank you for giving me valuable advice over the course of this entire project. Anne, thank you for always being available when I needed guidance while also allowing me to work independently and explore research topics that I am passionate about. Sylvain, thank you for teaching me about what it means to "get your hands dirty" in the lab and taking our ideas from the drawing board to an actual setup. The lessons I have learned from you both will serve me well into my future engineering career and for that I am eternally grateful. The financial assistance given by the McGill Faculty of Engineering and NSERC is also appreciated.

I would like to acknowledge the continued support from my lab mates from BSEL and CPPE. Nithin, thank you for teaching me about lasers and optics. Damon, your contributions to BSEL can't be overstated. Thank you for being a great office mate and offering advice with all aspects related to research. Dante, thank you for being my "go-to guy" from CPPE. Yuhan, Greg, Shashini, Teresa, Jerónimo, Phil, Lynn, Gemma, Lizbeth, Andrew, and Steven, thanks for always being so friendly in the hallways and offering to help me when I needed a hand.

I would like to thank the technical staff for helping me bring my ideas to fruition. Frank, you took me under your wing way back when I was an undergraduate student. Thank you for everything you have taught me about work and life in general. Ranjan, thank you for teaching me about what it takes to develop a methodology and to work diligently. Thank you to Gerald, Austin, Lisa, and Andrew for your continued support. I'd also like to extend my thanks to Angel, from FEMR, who was extremely friendly and helpful in taking microscopy images for this work.

Finally, I'd like to thank my family and friends. To my sisters, Claudia, Lori, and Sophia, thanks for being around to offer a listening ear when I needed it (even though you had no idea what my work was about). To all my friends in chemical engineering, thanks for all the gatherings and socials we had. Sometimes I needed a break from research, and I am glad I did not have to spend that time alone. I'd like to especially thank my friend Ali, who has been on this academic journey with me since 2018 when we met in CHEE 200. To my parents, mom and dad, thank you for everything you have given me. Without your support, values, and lessons I would not be the person I am today.

Author contributions

The contribution of the author for each section of the thesis is explained in Table 1.

Table 1: Summary of author contributions to each section of the thesis

Thesis section	Contribution
Introduction	Research regarding the necessity of this work was completed to give sufficient background knowledge for the project.
Literature Review	Pertinent literature regarding the subject matter of the thesis is compiled and summarized. Fundamentals of laser machining and technologies related to nanoparticle collection are presented.
Objectives	Based on the literature review and current state of this work, objectives for the research were laid out.
Methodology	Methodology regarding nanoparticle collection, recovered material quantification, and analysis methods are explained in detail.
Results and Discussion	Experimental results are shown using a series of figures and tables. Additionally, there is discussion regarding the explanation of the results and their implications.
Conclusion and future work	The main objectives of the work are revisited, and suggestions are provided for future work stemming from this project.

Table of Contents

List of Figures

List of Tables

List of Abbreviations

Abbreviation	Units	Description
NPs	-	Nanoparticles
F	J/cm^2	Laser pulse fluence
F_o	J/cm^2	Peak pulse fluence
F_{th}	J/cm^2	Ablation threshold fluence
N	pulses	Number of pulses
$F_{th}(N)$	J/cm^2	Ablation threshold fluence for N pulses
$F_{th}(1)$	J/cm^2	Single pulse ablation threshold fluence
E	J	Laser pulse energy
ω_o	μm	Theoretical beam diameter
P	mW	Laser average power
f	Hz	Laser pulse frequency
v	mm/s	Laser machining stage velocity
S	-	Incubation coefficient
PPS	pulses	Pulses per spot
Δx	μm	Distance between consecutive laser pulses
Δy	μm	Distance between the centers of two consecutive parallel laser machined lines
$\Gamma(x, y)$	J/cm^2	Accumulated fluence
N_r	-	Number of overscans
ϕ	J/cm^2	Local laser fluence
φ_{pulse}	%	Laser pulse overlap
φ_{line}	%	Laser ablated line overlap
ω_{eff}	μm	Effective beam diameter
$\eta_{collection}$	%	Nanoparticle collection efficiency
$m_{recovered}$	μg	Mass of material recovered from nanoparticle collection
$m_{removed}$	μg	Mass of material removed from surface by laser ablation
HEPA	-	High efficiency particulate air
x_i	-	Mass fraction of component i

m_i	µg	Mass of component *i*
Δt	ns	Time delay
min	-	Minutes
PVT	-	Position-velocity-time
CCRF	-	Capacitively coupled radiofrequency
CCP	-	Capacitively coupled plasma
DBD	-	Dielectric barrier discharge
SEM	-	Scanning electron microscope
TEM	-	Transmission electron microscope
STEM	-	Scanning transmission electron microscope
ICP	-	Inductively coupled plasma
OES	-	Optical emission spectrometry
MQL	-	Minimum quantification limit

1. Introduction

Sustainability and circular economy considerations have become increasingly relevant in a world that is trying to reduce waste from its manufacturing processes. From both an environmental protection and resource conservation standpoint, waste reduction is key. There are also additional benefits to waste recovery such as cost savings, regulatory compliance, and the development of long-term sustainable practices. Considering this, in 2022 the government of Canada published *The Canadian Critical Minerals Strategy* in which a framework for the recovery and re-purposing of industrial process waste is laid out. Laser surface machining is gaining more importance in industrial settings; however, the process comes along with the production of nanoparticles. These particles represent an important by-product yet they are mostly treated as a waste stream [1]. Efficient nanoparticle removal is essential to both ensure the quality of the laser textured surface and prevent inhalation of hazardous material. The industry standard for nanoparticle removal is a high efficiency particulate air (HEPA) filter. A drawback of these filters is that the recovery of nanoparticles from them is a resource and energy intensive process. If these particles were collected and recovered, they could be repurposed for use in applications such as catalysis, biomedicine, electronics, and nanofluids. In addition to their many uses, these nanoparticles present a financial opportunity as they are more expensive than their respective raw materials [2]. Additionally, a challenge that commonly arises in laser machining is dealing with the redeposition of nanoparticles on the laser textured surface. Therefore, efficient nanoparticle removal methods are imperative in ensuring the desired laser machined microstructure is maintained.

Joy and Kietzig previously demonstrated a proof-of-concept methodology for nanoparticle collection based on voltage application to a metal plate [3]. While the approach proved successful, the process is not optimized for collection efficiency, the collection mechanism is not fully understood, and the collected nanoparticles have yet to be characterized.

In this work, a novel nanoparticle collector design consisting of a rod-shaped electrode and a suction line is introduced. Its performance is assessed across a range of operating parameters to determine at which settings nanoparticle collection is optimized. Additionally, the effect of laser fluence and target material composition is investigated. As an extension to this work, a methodology for in-flight surface functionalization of metal nanoparticles is tested. By

functionalizing nanoparticles with an organic layer, their surface becomes stabilized reducing the agglomeration of individual particles.

Developing an efficient process of collecting nanoparticles can open doors for future research in characterizing nanoparticles based on laser settings. The wider outlook of this work is to develop a process for material recovery during laser machining as it would ultimately lead to reductions in the extraction of finite resources [4].

2. Literature Review

2.1. Femtosecond lasers in micromachining

Femtosecond lasers have found many applications in industries where control over optical, mechanical, wetting, and chemical properties of solid surfaces are required [5]. In a more general sense, laser surface machining can be used when micrometer or nanometer scale features are required on a surface [6]. Using femtosecond laser is convenient for generating surface structures because the exceptionally short pulse width allows for high peak beam intensity with low pulse energy [6]. Applications for which femtosecond laser machining is relevant include aeronautics [7], microelectronics [8], microelectromechanical systems (MEMS) [9], medical devices [10], and biomedicine [11]. Compared to other surface modification techniques, femtosecond laser machining is advantageous for several reasons:

i. Laser machining is contactless.
ii. Micro and nano scale structures can be fabricated in a single step.
iii. Laser settings can be easily adjusted to obtain a variety of structures.
iv. Laser machining can be done in a variety of environments where surface chemistry and contamination can be controlled. Additionally, laser machining can also be done in ambient conditions.

2.2. Femtosecond laser ablation of metals

The objective of the laser is to remove sufficient material to generate a desired surface structure (a process referred to as ablation). The ablation mechanism is dependent on material properties, laser settings, and the machining environment. Laser interactions with matter on the ultrashort pulse scale are complex because of the several processes taking place in such a short span of time. When a femtosecond laser pulse hits a sample, its energy is absorbed by the electrons over a thin layer which varies in thickness depending on the laser wavelength and target material [5]. The excitation of electrons occurs on a timescale of 100 fs [12]. For metals, thermalization of heated electrons causes the electron temperature to be higher than that of the lattice. This overall dynamic system is conveniently described as two sub-equilibrium systems: the hot electrons and the cold lattice [13]. The process by which this two-temperature system reaches an equilibrium is described by the two-temperature model and it occurs in a timespan of several picoseconds [14]. Processes occurring on a time scale longer than several picoseconds are considered thermal. Melting occurs

on the time scale of 100 picoseconds while material ablation can last as long as nanoseconds [5]. There are several mechanisms by which ablation may occur that are summarized in Table 2. Pulse duration and energy are the key factors that determine which ablation mechanism is dominant [15].

Table 2: Summary of ablation mechanisms

Mechanism	Description	References
Evaporation	The energy of atoms/ions of the target becomes higher than the atomic binding energy causing ablation in the form of evaporation of the material.	[16, 17]
Phase explosion	The surface of the target is heated above its critical temperature. The liquid metal sputters into a vapor that is instantly ejected from the surface.	[18, 19]
Spallation	High lattice temperatures cause pressure build up eventually leading to relaxation which causes particles to accelerate away from the ablation point. If the pulse duration and electron-phonon interaction time are both less than the mechanical relaxation time, material is ejected by spallation.	[20, 21]
Fragmentation	The target breaks down into fragments due to mechanical stress caused by rapid thermal expansion of the surface.	[22, 23]

Depending on laser machining parameters, the ablated material is ejected in a plume composed of atoms, ions, clusters, and nanoparticles. Once ablation is complete, the surface cools at a rate between 10^{13} and 10^{15} K/s [24].

2.3. Key process parameters for laser machining

The ablation threshold, F_{th}, is the laser fluence (for a given number of pulses and pulse duration) that provides sufficient energy to ablate a target. This threshold fluence is material dependent, and for long enough pulse durations, machining environment can also be a factor [25]. It has been previously determined that the ablation threshold can be expressed in terms of the peak fluence, F_o. For a beam with a Gaussian profile, the peak fluence is given by the following equation [12]:

$$F_o = \frac{8E}{\pi\omega_o^2}$$ Equation 1

where ω_o is the theoretical beam diameter and E is the single pulse energy given by the following expression [12]:

$$E = \frac{P}{f}$$ Equation 2

where P is the average power of the laser beam and f is the frequency (i.e., the pulse repetition rate).

In Equation 1, ω_o is the spot size according to the $1/e^2$ definition. This refers to the diameter at which the intensity is $1/e^2$ (~ 14%) of its peak value. Figure 1 is a graphical representation of the concept of the $1/e^2$ diameter definition.

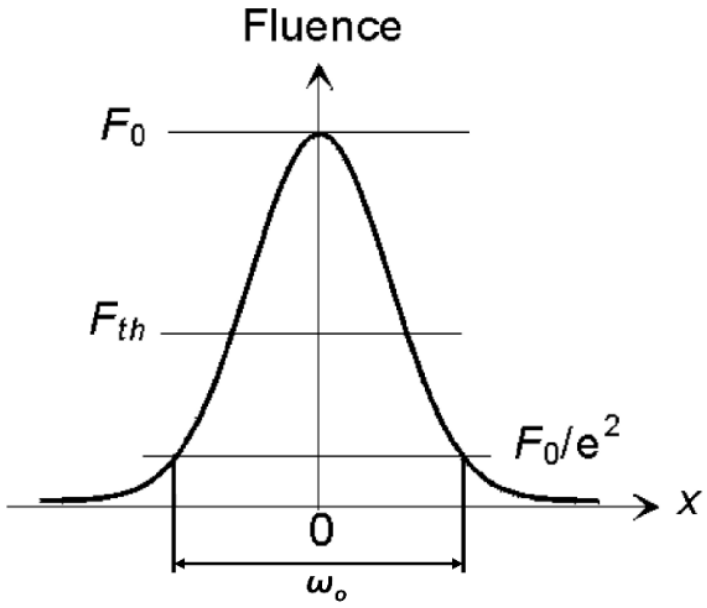

Figure 1: Diagram of fluence profile with $1/e^2$ beam diameter shown (adapted from [26]).

The accumulation model is used to examine the effect of cumulative laser action on an ablated sample. Using this model, the ablation threshold for any number of pulses, $F_{th}(N)$, is related to the single pulse ablation threshold, $F_{th}(1)$, by the following expression [27]:

$$F_{th}(N) = F_{th}(1) \cdot N^{S-1}$$ Equation 3

where N is the number of pulses and S is the incubation coefficient. The incubation effect is the altered absorption of laser pulses caused by the impingement of previous pulses. The degree to which incubation occurs is material dependent and is measured by the incubation coefficient [28].

When generating lines and patches of microstructures, the accumulation of pulses on a spot and along a line needs to be considered. The pulse accumulation is considered by the pulse per spot (PPS) parameter. For laser machining of a two-dimensional raster scan, the PPS is defined by the following expression [29]:

$$PPS_{total} = (PPS_x)(PPS_y) = \left(\frac{\omega_o}{\Delta x}\right)\left(\frac{\omega_o}{\Delta y}\right) \quad \text{Equation 4}$$

where Δx is the distance between two consecutive pulses in a line, and Δy is the distance between the centers of two consecutive parallel laser machined lines. Figure 2 illustrates the difference between Δx and Δy.

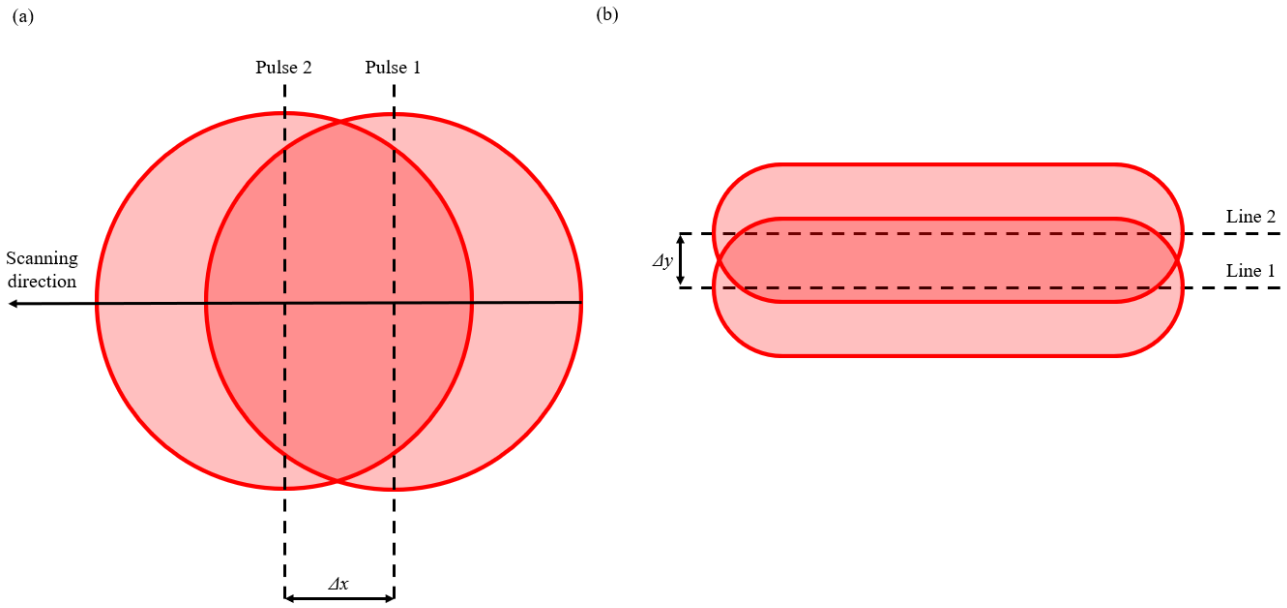

Figure 2: Schematic diagrams of (a) pulse overlap and (b) line overlap.

An accumulated fluence profile can be determined by summing individual Gaussian pulses (that are displaced by increments of Δx and Δy) over a reference area [29]. The accumulated fluence, $\Gamma(x, y)$, is given by the following double sum [30]:

$$\Gamma(x,y) = N_r \sum_i \sum_j \phi(x,y,i,j) \quad \text{Equation 5}$$

where N_r represents the number of over-scans (the number of times an ablated patch is scanned over). The i and j terms represent the number of beam displacements in the ablated area for x and y, respectively. The $\phi(x,y,i,j)$ term is the local fluence given by [30]:

$$\phi(x,y,i,j) = F_o e^{-2\left(\frac{\left(x+\frac{v}{f}i\right)^2+\left(y+\frac{v}{f}j\right)^2}{\omega_o^2}\right)} \quad \text{Equation 6}$$

In Equation 6, v denotes the scanning velocity.

The concept of pulse accumulation can alternatively be explained by pulse overlap (φ_{pulse}) and line overlap (φ_{line}). The pulse overlap in a laser machined line is a function of the scanning velocity, the frequency, and the beam diameter. The line overlap of a laser machined patch is a function of the effective beam diameter, ω_{eff}, and the user defined Δy. The pulse and line overlap are given by the following expressions [12]:

$$\varphi_{pulse} = \left(1 - \frac{v}{f\omega_o}\right) \cdot 100 = \left(1 - \frac{\Delta x}{\omega_o}\right) \cdot 100 \quad \text{Equation 7}$$

$$\varphi_{line} = \left(1 - \frac{\Delta y}{\omega_{eff}}\right) \quad \text{Equation 8}$$

where ω_{eff} is the effective beam diameter determined by the width of an ablated line. The effective beam diameter is different from the $1/e^2$ beam diameter, ω_o, which is determined from the beam intensity profile. The effective beam diameter is dependent on the ablation threshold of a material, and the laser machining settings and environment. [31].

2.4. Factors influencing nanoparticle generation

The production of nanoparticles by laser ablation is a simple process when compared to alternative methods. Benefits of using laser ablation for nanoparticle production include the absence of long reaction times, control over the machining environment, and absence of toxic chemicals [32]. Characteristics of the produced nanoparticles are influenced by both the surrounding environment and material properties of the target.

A key material property that influences nanoparticle generation is electrical conductivity of the target. This intrinsic material property indicates how well a material conducts electrical current. A

general trend that has been observed is that materials with a higher electrical conductivity are ablated more easily (they experience higher material removal from the surface) [3]. Ablation of a material with high electrical conductivity may lead to the ejection of electrons, causing a positively charged region to form on the target surface. This leads to a separation of charge which generates an electric field that acts as the driving force for the ejection of ions [33]. Therefore, it can be expected that targets with higher electrical conductivity will generate more nanoparticles, possibly leading to increased collection.

Although achieving a high enough fluence is required to generate nanoparticles, it is notable that fluence does not affect the size distribution of nanoparticles [34, 35]. The size distribution can however be affected by the laser beam profile contacting the surface (e.g., gaussian, ring shaped, or flat top beam profile). The beam profile determines how the pulse energy is distributed on the surface which in turn affects how the molten target material is agglomerated and ejected from the point of ablation [34, 36]. These dynamics can be explained by the Marangoni effect, mass transfer caused by a gradient in surface tension. Molten material temperature decreases radially outward from the laser irradiated area, causing mass transfer radially outward to the region of higher surface tension [37]. Cooling of the ejected material leads to the formation of nanoparticles. Another factor that can influence the nanoparticle size distribution is the sample thickness. Specifically for thin metallic films, a decrease in thickness leads to a shift towards size distributions with lower mean values due to reduced laser-induced stresses on the surface [38].

2.5. Nanoparticle plume behavior

During laser micromachining, material removal results in the formation of an ablation plume. This plume is composed of two main parts: a faster moving atomic/plasma plume consisting of neutral and ionic species and a slower moving nanoparticle plume [39]. At low pressures (on the scale of 1000 Pa or lower), the atomic/plasma and nanoparticle plumes have expansion velocities on the scale of 10^4 m/s and 10^2 m/s, respectively [40]. In machining environments close to atmospheric pressure, the plume becomes confined to the target surface. This confinement leads to a slower plume expansion velocity on the scale of 10 m/s [41]. Nanoparticles are the main component of the ablation plume, comprising of 80 to 90% of the total ablated mass (the remaining being atoms and ions) [42].

Additionally, during ablation of a sample, both the atomic/plasma plume and the nanoparticle plume can interact with the incident laser beam. This interaction is especially present when high repetition rates and pulse overlaps are used, where the plume generated by a single laser pulse may interact with the subsequent laser pulses [43]. When a laser beam has a fluence higher than that of the ablation threshold of the target, the plasma plume is formed. If the plasma reaches a high enough density, it can absorb laser energy causing the ablation process to be less efficient. This process is referred to as plasma shielding since the plasma shields the target from the next incoming laser pulses [44]. If the efficiency of laser ablation is reduced, material removal from the surface would become a thermally dominated process where a melt layer is formed and ejected [45, 46]. Nanoparticles in the ablation plume can also interact with the incident laser beam. They can absorb and scatter the incoming light causing the effective beam intensity at the surface to decrease [44, 47, 48].

Laser fluence can affect the dynamics of ablation plume expansion. A commonly observed phenomenon during laser ablation is the spatial separation between the fast-moving atom/ion portion and the slower moving nanoparticle portion of the ablation plume [49]. As laser fluence increases, the separation between the two portions increases due to a higher degree of charge separation in the plume causing further ejection of the atom/ion portion from the ablation point [50]. The overall shape of the ablation plume can be affected by laser fluence dependent plasma shielding effects. With increased fluence, a more energetic plasma plume is formed leading to the absorption of more laser energy. Additionally, particles generated by the laser are ejected further from the ablation point with increasing fluence [49, 51].

Plume deflection is a phenomenon that has been observed during laser machining, however, it is not fully understood. This occurrence is most evident in laser machining setups where the beam remains stationary while translational stages move the target sample under the beam to generate patches of surface structures. At high enough velocities, the stage movement can generate a fictitious force on the nanoparticle plume causing a deflection in the direction of motion [3].

2.6. Nanoparticle collection methods

Although they are not as widely studied when compared to other aspects of laser machining, there are several known methods for nanoparticle collection.

The method of collection can vary depending on the laser machining environment. If laser machining is performed in a liquid environment, nanoparticles can be collected in the form of a colloid. The colloid is formed by the expanding nanoparticle plume which is surrounded by the liquid (i.e., the nanoparticles are produced within the liquid). The surrounding liquid has a stronger effect of confining the ablation plume when compared to a gaseous environment [32]. This confinement causes more rapid quenching of the plasma plume leading to the produced nanoparticles having a size distribution with a lower mean diameter [52]. Collection in a liquid environment can also be done using an electrode system where nanoparticles can be deposited through the application on an electric field [53]. If machining occurs in a gaseous environment (atmospheric pressure or lower), nanoparticles can be collected as nanopowders. There exist designs for closed ablation chambers that are interfaced with other containers or chambers (for collection) which all have the same general working principle (closed chambers are used to avoid the loss of nanoparticles to the environment). A target is placed in the chamber and ablated while an inert gas flow, parallel to the target, pushes the produced nanoparticles towards the chamber outlet. The nanoparticles are then collected in the container that is connected to the ablation chamber outlet [32]. An advantage to machining in a controlled gaseous environment is that the surroundings can be tuned in a way to slow down the expansion of the nanoparticle plume [40, 54].

More recently, glass substrates have been used to collect nanoparticles [41]. This works by placing a glass plate in front of the target being ablated. The laser irradiation of the target can then occur through the glass. By using a short enough distance between the glass plate and the target material, the ejected nanoparticles can be collected on the glass. It is important to note that this method of collection has only been used for small amounts of nanoparticles where the focus is to analyze them using microscopy techniques [34]. Although this method is not suitable for excessive collection, it benefits from not requiring the use of a highly controlled laser machining environment.

The use of a floating potential or an electric field have also proven to be effective methods of nanoparticle collection [3]. The techniques uses a metal plate placed near the point of laser ablation. For collection using a floating potential, a potential is applied to the metal plate. To perform collection using an electric field, a potential is again applied to the collector plate while

the target material is grounded. As the applied potential is increased, the nanoparticle collection on the metal plate is more confined regardless of the method used. For a fixed applied potential, the nanoparticle confinement on the collector plate is greater for the electric field technique. This result is attributed to the steady local electric field between the collector plate and target (while the floating potential collection method is not electrically well defined). It was also observed that the amount of collected nanoparticles directly correlated with the electrical conductivity of the target material (i.e., more nanoparticles were collected for materials with higher electrical conductivity). Like the glass substrate technique, this method of collection can also be used in uncontrolled environments. An additional benefit to this method is that it can be used for the collection of quantifiable amounts of nanoparticles.

2.7. Capacitively coupled plasma

Capacitively coupled plasma (CCP) is generated by using an electrode configuration that resembles a capacitor. One electrode is connected to a high voltage power supply while the other is connected to ground. The electric field causes the gas between the two electrodes to ionize, and electrons are released. Electrons in the gas are further accelerated by the electric field leading to collisions that produce secondary electrons. If the electric field is strong enough, an electron avalanche will occur after which the gas becomes conductive due to the presence of free electrons [55]. CCP is commonly used for etching, film deposition, and surface functionalization [56]. Depending on the application, CCP can have different electrode configurations such as parallel plates, barrel reactor, end-electrode cylindrical, and ring-coupled cylindrical [57].

2.8. Dielectric barrier discharge

A dielectric barrier discharge (DBD) is a plasma generated by applying a high voltage of alternating current between two electrodes that are separated by a dielectric material. The dielectric material prevents arcing between the electrodes, and in some cases, an electrode can be encapsulated or coated in dielectric material. If the applied voltage is high enough, plasma discharges between the two electrodes will form. Due to the dielectric barrier, the plasma discharges pulsed short-lived events. The frequency and duration of these discharges is dependent on the applied voltage [58]. Compared to other plasma sources, DBD is advantageous because it can be operated at atmospheric pressure, it allows for localized discharges, requires relatively low

energy, and has a wide range of applications. Applications of DBD include ozone formation, sterilization, surface functionalization, and biomedicine [59, 60].

2.9. Nanoparticle functionalization

Due to their high surface to volume ratio, nanoparticles quickly interact with their surroundings to achieve stability, resulting in the formation of aggregates [61]. Nanoparticle surface functionalization plays a key role in stabilizing these reactive particles so that they can be used and transported easily.

The employment of plasma for nanoparticle functionalization offers notable convenience due to its inherent high energy. Components of the plasma such as electrons, ions, and free radicals interact with the nanoparticle surface leading to effective surface activation. Once the surface is activated, functionalization can occur by chemical reaction, physical adsorption, and thin film deposition [62].

In-flight functionalization is a process where particles and a reactive gas are passed through a plasma with the goal of applying a coating to the particles. DBD plasma torch reactors have been developed for in-flight functionalization of metal nanoparticles. This technique is advantageous because it can be used at atmospheric pressure and achieves a high throughput [63]. The reactor used a quartz tube as the dielectric and three pairs of electrodes along its length. An applied alternating voltage of 13 kV was used with a frequency of 20 kHz. Helium with some argon added was used as the carrier gas. To generate the coating, ethylene, butadiene, pyrrole, and acetylene were used as precursors. The rate of coating deposition on the particles was dependent on both the precursor used and whether injection occurred in the plasma discharge or afterglow.

Capacitively coupled radiofrequency (CCRF) plasma reactors have also been used for in-flight functionalization of copper nanoparticles [64, 65]. Rather than injecting the particles, both the synthesis and functionalization occur in the same reactor. The nanoparticles are synthesized in argon by the erosion of a copper cathode by a low-pressure pulsed arc system. The synthesis is followed by in-flight functionalization in the cylindrical CCRF portion of the plasma reactor. The CCRF plasma is applied to the stream of nanoparticles and argon while ethane is injected to produce the organic coating. The optimal conditions to produce organically coated nanoparticles were an arc pulse frequency of 6-8 Hz, peak pulsed arc current of 30-40 A, and a radiofrequency power level of 40-80 W. A capacitively coupled electrode frequency of 13.56 MHz was used. The

argon gas flow rate was between 200-300 sccm while the ethane flow rate was 2 sccm. The reactor pressure was kept between 2-4 Torr (267-533 Pa) to maintain the operating conditions for the synthesis and functionalization processes. Using these settings, nanoparticles on the size scale of 50 nm were produced with a polymer-like coating with thickness of 3-10 nm. This reactor design is advantageous because it prevents agglomeration and contamination of the bare nanoparticles.

3. Objectives

While there are successful nanoparticle collection methodologies available, most of them have not been optimized for the collection and recovery of nanoparticles produced during laser micromachining. In industrial settings, combined collection and recovery methods are not widely used at this point. Additionally, the collected nanoparticles have yet to be characterized. Therefore, it is hypothesized that by adjusting nanoparticle collection process parameters, the nanoparticle collection efficiency can be maximized. Additionally, to make a useful product from the produced nanoparticles, an in-flight functionalization methodology will be tested. To verify the stated hypothesis, this thesis will address the following objectives.

(1) Study nanoparticle collection by adjusting collection process parameters: A three-level factorial design of experiment approach will be taken to assess the effect of gas suction flow rate and translational stage velocity, for a fixed laser fluence. To further assess the functionality of the collection process, its performance will be compared to an in-line HEPA filter. Collection efficiency will be assessed by comparing material removal to nanoparticles collected.

(2) Investigate the effect of laser fluence on collection efficiency: Once optimal collection parameters have been determined for a single laser fluence, their applicability will be tested across a range of fluence settings. For a fixed set of nanoparticle collection settings, fluence dependent ablation plume dynamics may affect the efficiency of the collection.

(3) Determine the effect of material composition on collection efficiency: To determine whether the presence of multiple elements affects collection efficiency, alloys will be ablated alongside a selection of pure metals. The collection efficiency the main element of each alloy will be compared to that of pure metal ablation. For example, the collection of iron will be compared when pure iron and stainless steel are used as the target material. Additionally, the collection efficiency of the main components in each alloy will be compared. Again, considering the example or stainless steel, the collection of iron, chromium, and nickel will be compared.

(4) Test a methodology for in-flight functionalization of metal nanoparticles: To achieve nanoparticle surface stabilization, a method for in-flight functionalization of metal nanoparticles will be tested using a CCRF-DBD plasma reactor.

4. Methodology

4.1. Laser System

The samples were ablated using an amplified Ti: Sapphire solid-state laser system (Libra, Coherent Inc., Santa Clara, CL, USA) having a Gaussian beam profile, wavelength of 800 nm, pulse duration of ~100 fs, and a frequency of 1000 Hz. The laser pulse energy was adjusted to the desired level using a computer-controlled attenuator. The beam was focused onto the sample surface using a plano-convex lens with a focal length of 200 mm. The samples were mounted to a 2D translational stage (Newport Corporation, Irvine, CL, USA) to be machined under a stationary laser beam. The velocity and trajectory of the stages was controlled using a PVT trajectory file that was fed to a stage motion controller (XPS, Newport Corporation). A raster scan trajectory was used to ablate the samples.

4.2. Laser machining settings for nanoparticle collection

4.2.1. Fluence

To allow for comparison between different collection settings and materials, substrates were ablated using a fluence that was a constant multiple of the ablation threshold. Using such a fluence avoided variability caused by laser interactions with the nanoparticle plume. For the experiments, a fluence equal to 4.5 times the ablation threshold was chosen to ensure ample nanoparticle production for quantification. For the experiments related to the second objective, multiples of the ablation threshold of 3.0, 4.5, 6.0, and 7.5 were used.

Although using a constant multiple of the ablation threshold is the standard method of comparing the ablation of different materials, there are limitations. These limitations include the varying spot size for different fluence settings and the varying plasma plume characteristics.

4.2.2. Ablation threshold determination

There are several techniques that can be used to determine the ablation threshold such as the diameter method and the maximum depth method. For this thesis, the diameter method was used since the diameter of an ablated crater can be measured with more confidence than the maximum depth of a crater. Since the diameter is measured with more confidence, the ablation thresholds determined using this method can be considered more accurate [66].

The diameter method takes advantage of the following relationship to determine the ablation threshold of a given material [67, 68]:

$$\omega_{eff}^2 = 2\omega_o^2 \ln\left(\frac{F_o}{F_{th}}\right) \qquad \text{Equation 9}$$

Using a specified number of pulses, a line can be ablated on a sample surface. Next, by plotting ω_{eff}^2 versus the natural logarithm of F_o (calculated using Equation 1), both ω_o and F_{th} can be extrapolated. Figure 3 is an example of such a plot (with varying number of pulses) that was generated for copper.

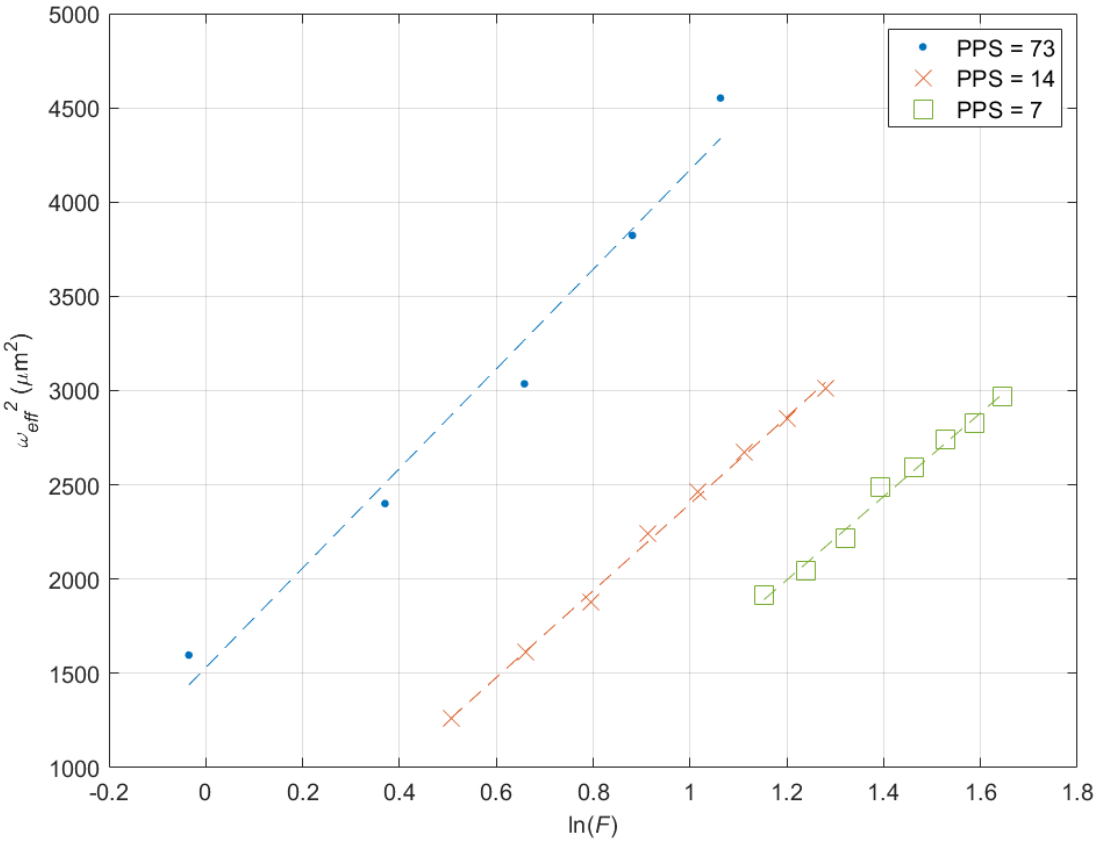

Figure 3: Diameter method plot for F_{th} determination of copper at varying PPS settings.

Using this method, the ablation threshold for all metals used for this work were determined and are given in Table 3.

Table 3: Ablation threshold for chosen target metals

Metal	Stage velocity [mm/s]	F_{th} [J/cm^2]
Copper	1	0.56
	5	0.96
	10	1.35
Brass 360	1	1.12
Iron	1	1.90
Stainless steel 304	1	2.16
Aluminum	1	1.81
Aluminum 6061	1	1.53

4.2.3. Patch size and line overlap

A laser machined raster scan patch size of 2 mm × 2 mm was chosen. This size selection was based on results from preliminary testing where it was noted that a sufficient mass of nanoparticles was generated for quantification (on the scale of μg). A line overlap of 95% was used to generate the patches (see Equation 8). Using a high overlap resulted in a uniform depth of the ablated area due to the homogeneous fluence profile over the ablated area.

4.3. Target material selection

To determine the optimized collection process parameters and assess the effect of laser fluence, copper (110 grade, 99.9% pure) was used as a target material. This target material was chosen because it has previously been used in laser machining [69, 70]. Copper II oxide (Copper(II) oxide, nanopowder, Thermo Scientific Chemicals, 50 nm size) nanoparticles were used to test the in-flight functionalization methodology since they are commonly produced from laser machining copper in air. To investigate the effect of material composition on collection efficiency, three commonly used alloys in laser machining industry were chosen. They are summarized in Table 4.

Table 4: Summary of alloys used for nanoparticle collection experiments to assess the effect of target material composition

Alloy	Grade	Alloy applications	Main component	Other components of interest	Trace elements	References
Brass	360	Electronics and plumbing	Cu	Zn	Fe, Pb, Si	[71]
Stainless steel	304	Medical devices and life sciences	Fe	Ni, Cr	C, Co, Cu, Mn, Mo, N, P, Si, S	[72, 73]
Aluminum	6061	Aerospace	Al	Cr	Cu, Fe, Mg, Mn, Si, Ti, Zn	[74, 75]

The mass percentage of the main components in each alloy are presented in Table 5. To obtain a reliable measurement of the composition, five distinct replicates of each alloy were analyzed by ICP-OES (refer to section 4.5.1 for more details regarding ICP-OES).

Table 5: Mass percentages of main components in alloys under investigation

Alloy	Component	Mass percentage [%]	Standard deviation [%]
Brass 360	Cu	61.5	0.3
	Zn	38.5	0.3
Stainless steel 304	Fe	72.6	0.2
	Cr	18.4	0.1
	Ni	9.0	0.3
Aluminum 6061	Al	99.8	0.04
	Cr	0.2	0.04

4.4. Nanoparticle collector

The nanoparticle collection experiments occurred in air. The main components of the nanoparticle collector are the high-voltage electrode, the grounded outer tube, and the plastic union tee that is connected to a suction pump (Gast Manufacturing Model DAA-V507-GB). Figure 4 a) shows a front view of the nanoparticle collector with all the key components labelled and Figure 4 b) focuses on the rod-shaped electrode.

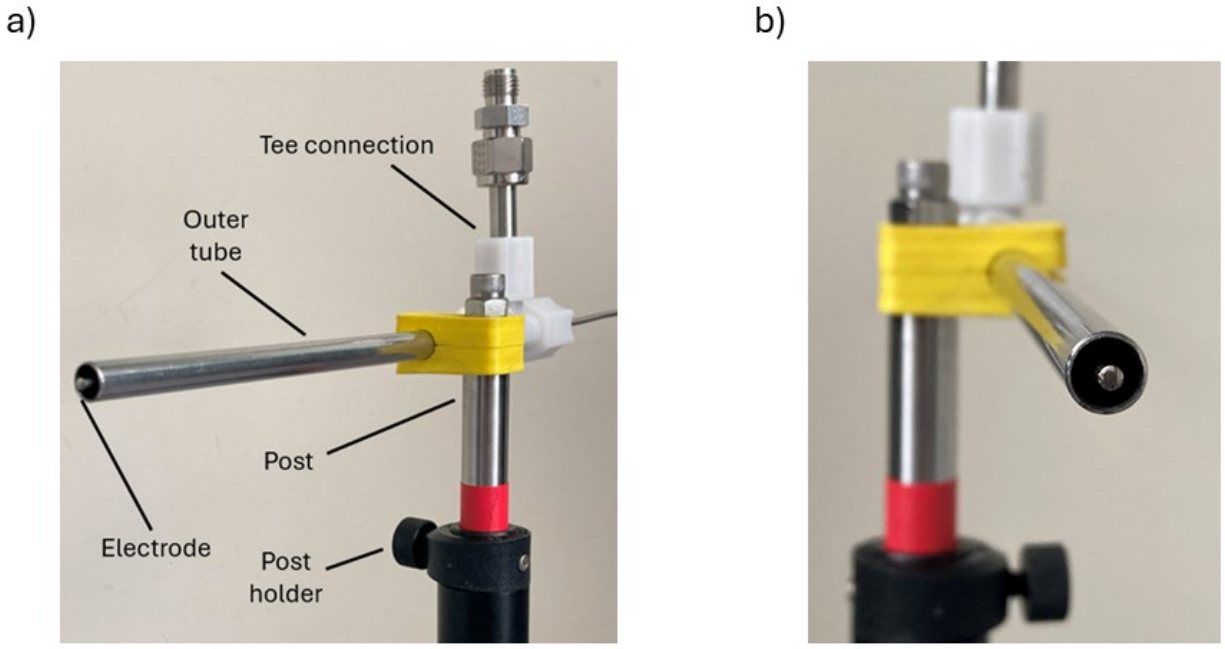

Figure 4: Nanoparticle collector a) side view with main components labelled and b) zoomed in front view of electrode

Using a post holder and a clamp, the collector was fixed at the desired position on the laser table. The post holder was used to adjust the collector 2 mm above and parallel to the target surface. The collector was positioned 3 mm beside the ablation point, aligning the electrode with the point of ablation. The collector was also positioned perpendicular to the direction of raster scanning as depicted in Figure 5.

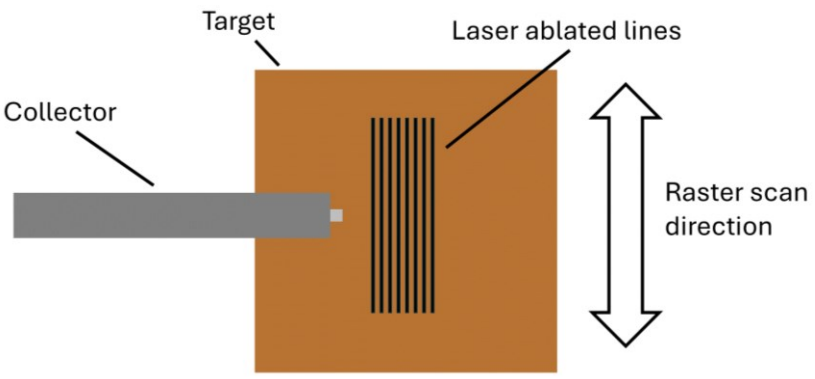

Figure 5: Collector position relative to direction of raster scanning

Figure 6 depicts how the collector was mounted next to the 2D translation stages. A 3D printed plastic separator piece is inserted between the electrode and the outer tube to ensure they did not make physical contact leading to a short circuit. Once in position, the vacuum pump tube was connected to the vacuum connector. The live terminal of the DC power supply (Fluke 412B High Voltage Power Supply) was connected to the back end of the high-voltage electrode and its ground to the outer tube. After the connections have been made, the vacuum pump was turned on and adjusted to the appropriate flow rate. The power supply was set to apply a potential of 2.0 kV to the electrode.

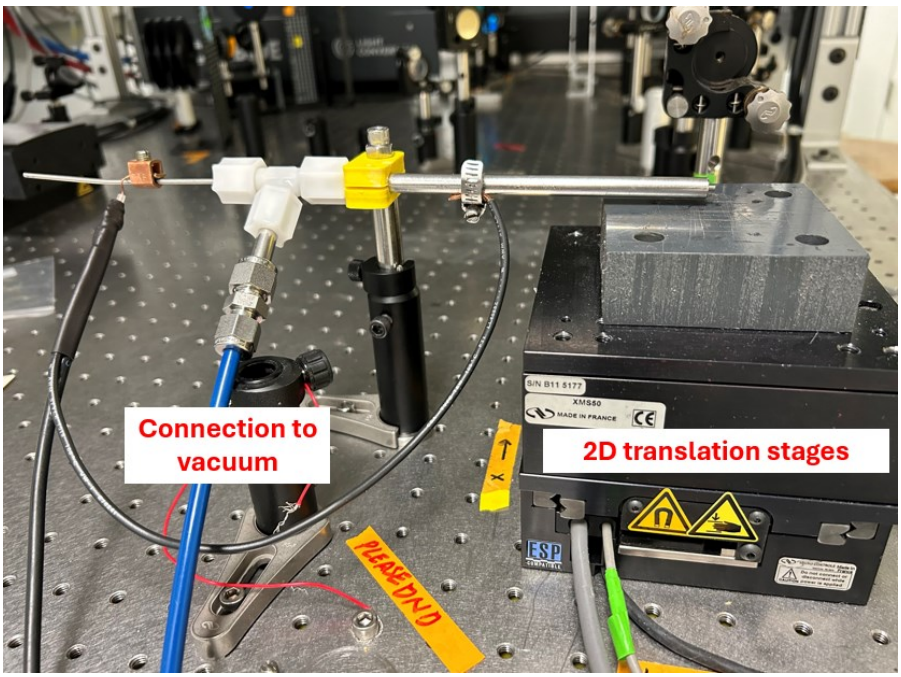

Figure 6: Collector mounted on laser table next to 2D translation stages

Once laser machining and collection was complete, the nanoparticles were rinsed off the collector into a digestion vessel using acetone. To ensure removal of all the recovered material, the electrode and outer tube were sonicated inside the digestion vessel for 10 min in a sonication bath (Branson 1510 Ultrasonic cleaner). Acetone was chosen because it can easily be evaporated when comes the time to digest the nanoparticles for further analysis. In addition, it is a commonly used chemical solvent that all collection apparatus components are resistant to. For each target material and set of nanoparticle collection settings, three replicates of the above-mentioned process were performed. In all graphs presented, error bars are used to signify one standard deviation from the mean (unless otherwise specified).

4.5. Analysis methods

4.5.1. Inductively coupled plasma – optical emission spectroscopy

Inductively coupled plasma (ICP) – optical emission spectrometry (OES) is a technique used to determine the amount of a certain element in a sample based on the emission of radiant energy by atoms. An ICP in argon provides high temperatures (up to 7000 K) necessary to vaporize and excite the atoms of a sample being analyzed. When the excited atoms undergo electronic deexcitation, photons are emitted in the UV-visible range. The number of photons emitted (i.e., the intensity) is related to the concentration of atoms in the sample [76, 77]. The main drawback of ICP-OES is the difficulty in preventing spectral overlap. Since elements usually emit light at several wavelengths, unaccounted spectral overlap can cause inaccuracy in optical emission intensity measurements [78]. For this project, ICP-OES (Thermo ICAP 6500 Series ICP-OES) was used to determine the mass of recovered metal from nanoparticle collection and to obtain accurate measurements of the previously mentioned alloys' composition.

To prepare the samples of recovered material for ICP-OES analysis, the organic solvent was dried from the sample using a light stream of nitrogen gas. Once dried, the metal was digested using 2-4 mL of 4% nitric acid. To aid the digestion process, samples were heated to 95 °C for two hours in a graphite digestion block with a built-in heater (SCP Science DigiPrep Jr.). After digestion, samples were left to cool to room temperature. Once cooled, the digested samples were completed to a Class A volume of 50 mL using deionized water. To avoid any unexpected contamination to the instrument, the samples were vacuum filtered (SCP Science DigiFilter 0.45 micron) prior to analysis. Using calibration standards of known metal concentration, a calibration curve relating

the concentration of metal to the intensity of emitted light was built. Figure 7 is an example of a calibration curve for copper showing the wide dynamic linear range from 0.1 to 100 ppm.

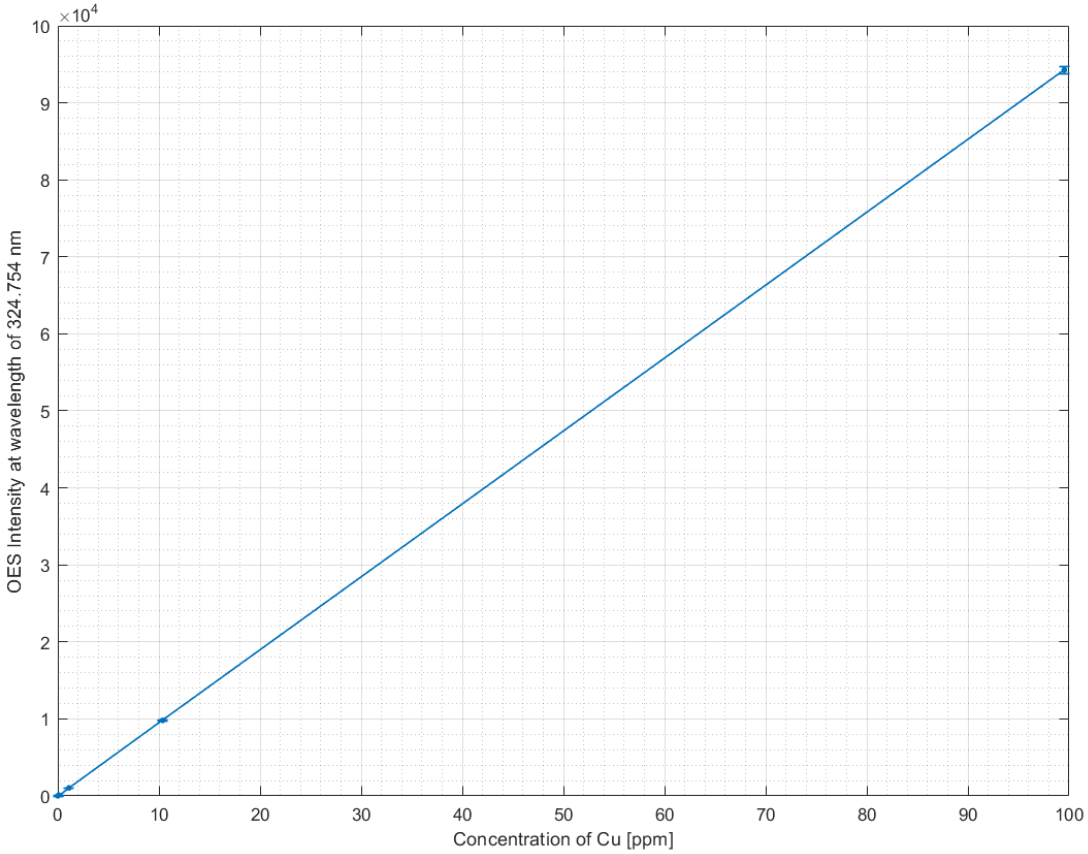

Figure 7: ICP-OES calibration curve for copper in nitric acid

To prepare the alloy samples, the previously mentioned steps were used. However, the stainless steel 304 and aluminum 6061 were digested in aqua regia, a 2:1 mixture of hydrochloric acid and nitric acid (the use of nitric acid alone was not capable of dissolving these alloys). Digestion was aided by heating to 95 °C for three hours using the same graphite digestion block mentioned prior.

The minimum quantification limit (MQL) is the lowest concentration of an element that can be reliably detected and quantified. This limit is calculated based on the element being analyzed and the method used to digest the sample [76]. Table 6 lists the MQL for all elements analyzed by ICP-OES.

Table 6: Minimum quantification limit for elements considered in ICP-OES analysis

Element	MQL [ppb]
Al	37.0
Cr	8.0
Cu	5.0
Fe	7.0
Ni	1.0
Zn	1.0

4.5.2. Confocal microscopy

Confocal laser scanning microscopy is a technique that uses light reflected from a focused laser beam to obtain high depth resolution of a sample. To illuminate the sample, a system of lenses is used to focus the laser light. Once the sample is illuminated, reflected light is collected from the same lens used for illumination. A pinhole aperture is placed in front of the detector to permit light from the focal plane, thus spatially filtering the out of focus light [79]. With optimal performance, confocal laser scanning microscopy has a depth resolution of ~0.8 μm and lateral resolution of ~0.3 μm [80]. For this work, confocal microscopy (Olympus LEXT OLS5000) was used to determine the depth of laser ablated patches. Having an accurate measurement of the laser machined patch depth was essential for determining the mass of material ablated by the laser. A benefit of using confocal microscopy is the reduced time of taking depth measurements for many samples when compared to other profilometry techniques. Figure 8 illustrates a depth profile that can be obtained using confocal microscopy. The drawback of using confocal microscopy was obtaining an accurate profile of the bottom of the laser ablated area. Since the laser ablated area had considerable depth (on the scale of 10 to 100 μm), the bottom of the patch was usually out of focus during imaging introducing noise into the measurement. This could have resulted in either an over or under estimation of the patch depth. Noise reduction processing of the images was used to improve the measurements; however, the accuracy may have still been affected.

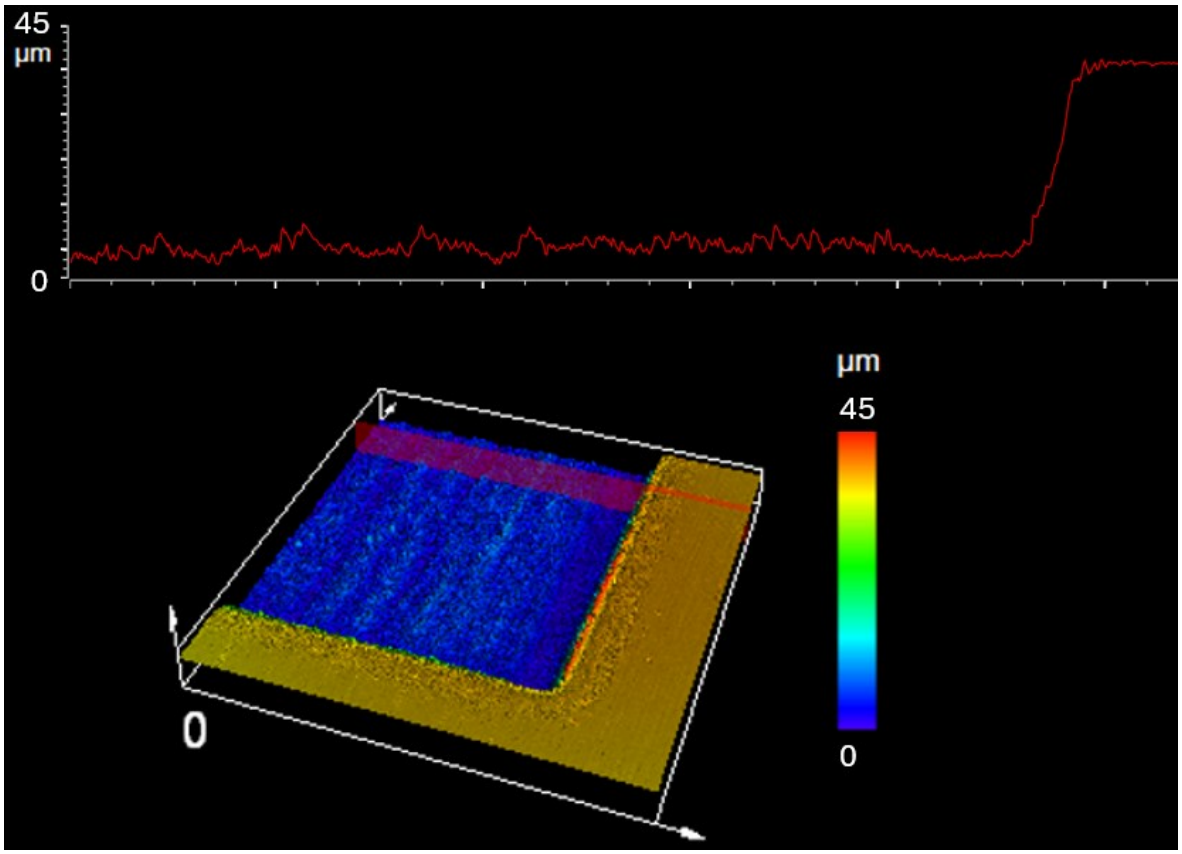

Figure 8: 3D image and depth profile of laser ablated patch on copper

4.5.3. Scanning electron microscopy

Scanning electron microscopy (SEM) works by generating a high energy electron beam from an electron source. The beam passes through electromagnetic lenses to ensure it remains narrow and focused. Once electrons strike the sample, several emissions are generated such as elastically scattered electrons, secondary and backscattered electrons, and X-rays. Various detectors are used to detect each type of emission generated from the interaction of electrons with the sample. The detected signals are processed to produce an image with high resolution and depth of field [81]. For this work, SEM (FEI Quanta 450 Environmental Scanning Electron Microscope) was used to analyze redeposited nanoparticles on the target material surface after laser ablation. The SEM used for this work operated with an ultimate resolution of 2 nm.

4.5.4. Transmission electron microscopy

Transmission electron microscopy (TEM) works by generating an electron beam inside a vacuum chamber. Electromagnetic lenses direct and focus the beam onto the sample being analyzed. Samples analyzed by TEM are very thin, with a thickness of ~100 nm. Electrons interact with the

sample without significant energy loss and are transmitted through it. The transmitted electrons are focused onto a detector to produce an image showing the areas of varying electron density within the sample. TEM produces high resolution images with resolution on the atomic scale [81]. For this work, TEM (ThermoFisher Talos F200X G2 (S)TEM microscope) was used for the analysis of laser generated iron and stainless steel nanoparticles. Additionally, TEM was used to analyze copper oxide nanoparticles that were passed through the plasma reactor for in-flight functionalization. The TEM used for this work has a resolution of 0.10 nm.

4.5.5. Scanning transmission electron microscopy

Scanning transmission electron microscopy (STEM) is a hybrid technique between SEM and TEM. An electron beam is generated and focused onto a sample. Like SEM, STEM also uses a raster scanning pattern to expose the sample to the electron beam. Electrons that interact with the atoms of the sample are either scattered or transmitted. Based on these interactions, several detectors are used such as bright field detectors (to detect transmitted electrons) and annular dark field detectors (to detect scattered electrons). Signals from these detectors are converted into images where each pixel of the image represents a point scanned by the electron beam [82]. The interaction of the electron beam with the sample also leads to the emission of characteristic X-rays of the elements present in the sample. Therefore, STEM is commonly used in conjunction with energy dispersive x-ray spectroscopy (EDX) providing elemental information on the sample. Using STEM with EDX is also convenient for generating elemental maps of a sample. For this work, STEM with EDX (ThermoFisher Talos F200X G2 (S)TEM microscope) was used to analyze multi-element nanoparticles produced from the laser ablation of stainless steel alloy. The STEM used for this work has a resolution of 0.16 nm.

4.6. Collection efficiency calculation

For a fixed set of process parameters, the effectiveness of the collection was quantified by an efficiency calculation. The collection efficiency is the fraction of the total mass of material removed from the surface by laser ablation that is recovered by the collector and is given by Equation 10.

$$\eta_{collection} = \frac{m_{recovered}}{m_{removed}} \qquad \text{Equation 10}$$

where $\eta_{collection}$ is the collection efficiency, $m_{recovered}$ is the mass of material recovered, and $m_{removed}$ is the mass of material ablated by the laser.

Although this calculation was practical for comparing collection between different process settings, it was not a perfect measure of the nanoparticle collection effectiveness. Losses during the recovered material quantification may have occurred from the electrode cleaning and ICP-OES sample preparation steps leading to a potential underestimation of the collection efficiency. Regarding analysis methods, both confocal laser scanning microscopy and ICP-OES were adequately sensitive to make reliable measurements to determine the mass of removed (patch depth measurement) and recovered (concentration measurement) material respectively. However, due to the previously mentioned limitation of each analysis methods, it is possible inaccuracies were introduced which may have influenced the collection efficiency calculation.

4.7. In-line HEPA filter

For the collection experiments using the in-line HEPA filter (McMaster-Carr Tube Stem In-line filter Style D), the same collector mentioned above was used. No potential was applied to the electrode. However, the vacuum pump was used for suction of the ejected material to the filter. To assess the effectiveness of the HEPA filter, a similar calculation to Equation 10 was used. The mass of copper oxides trapped in the filter was measured by weighing the filter before and after a laser machining run. Therefore, it was assumed that any change in weight of the filter was attributed to the collection of laser-generated copper oxide nanoparticles. In previously published work, it has been determined that the most common laser generated copper oxides in air are CuO and Cu_2O [83, 84]. Based on this, an upper and lower estimate of the amount of copper collected in the filter was determined from the mass fraction of copper in each of the oxides. Table 7 indicates the mass fraction of copper in each of the laser-generated copper oxides.

Table 7: Mass fraction of copper in CuO and Cu_2O

Copper oxide	Mass fraction of copper	Estimate
CuO	0.799	Lower limit
Cu_2O	0.888	Upper limit

From all this information, the collection efficiency of the in-line filter is given by Equation 11.

$$\eta_{HEPA} = \frac{x_{Cu} \cdot m_{Cu\ oxide}}{m_{removed}} \quad \text{Equation 11}$$

where x_{Cu} is the mass fraction of copper in the respective copper oxide, $m_{Cu\ oxide}$ is the mass of copper oxide collected in the filter, and $m_{removed}$ is the mass of material ablated by the laser. For a fixed set of collection settings, three replicates were performed using the in-line filter.

Using the dimensions of the laser ablated patch (length, width, and depth) and the density of pure copper, the ablated mass was calculated. It was assumed that the thickness of the native oxide layer of the copper was negligible since it was orders of magnitude lower than the laser ablated depth (i.e., ~10 nm versus ~50 μm) [85].

4.8. Assessment of collector performance using re-entrant structures

To further assess the performance of the nanoparticle collector, it was tested on a 5-axis (three translation stages and two rotational stages) stage setup used to produce re-entrant surface structures. Compared to the conventional straight wall structure, re-entrant structures have an overhang which enhances liquid repelling abilities and robustness [86]. The drawback with re-entrant structures is the difficulty in producing them. There is presently no repeatable and scalable manner to produce re-entrant structures outside of a clean room environment. 5-axis laser machining is a promising technique, however, the overhanging aspect of re-entrant structures presents a challenge. As material is ablated from the surface and ejected in all directions, nanoparticles can become trapped in the pore by the overhanging wall. The nanoparticles can either accumulate at the bottom of the pore or along the side walls. This accumulation leads to issues in producing a well-defined surface structure. To produce re-entrant structures with sufficient depth, width, and length (on the scale of 10 to 100 μm), efficient nanoparticle removal mechanisms are required. Therefore, it was determined that using the collector to produce re-entrant structures was a convenient test for its nanoparticle removal ability.

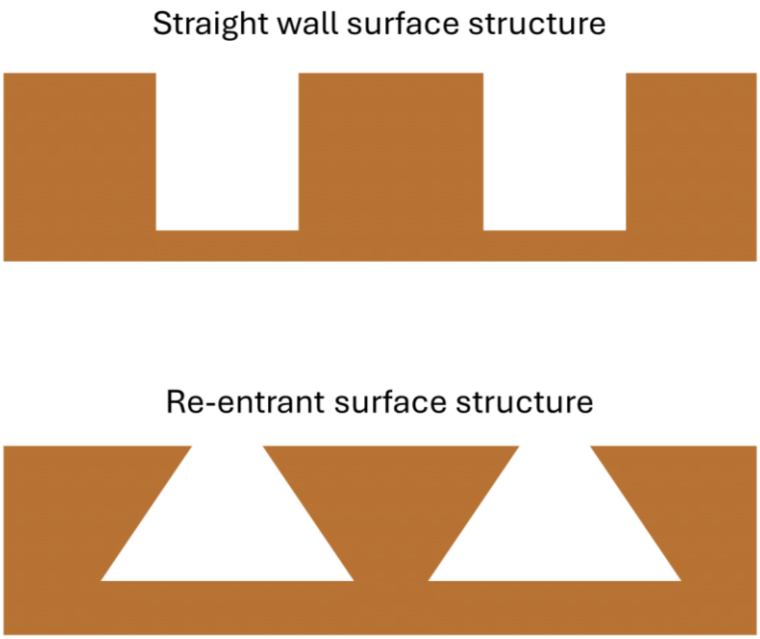

Figure 9: Schematic showing the difference between straight wall and re-entrant surface structures

The collector was mounted on a vertical breadboard as shown in Figure 10 a). Unlike for the experiments done using the 2D translational stages, the collector is slightly tilted at an angle of 8 degrees to avoid any collisions with the bulkier 5-axis stage setup. Additionally, the collector was positioned perpendicularly relative to the laser ablated re-entrant lines as shown in Figure 10 b).

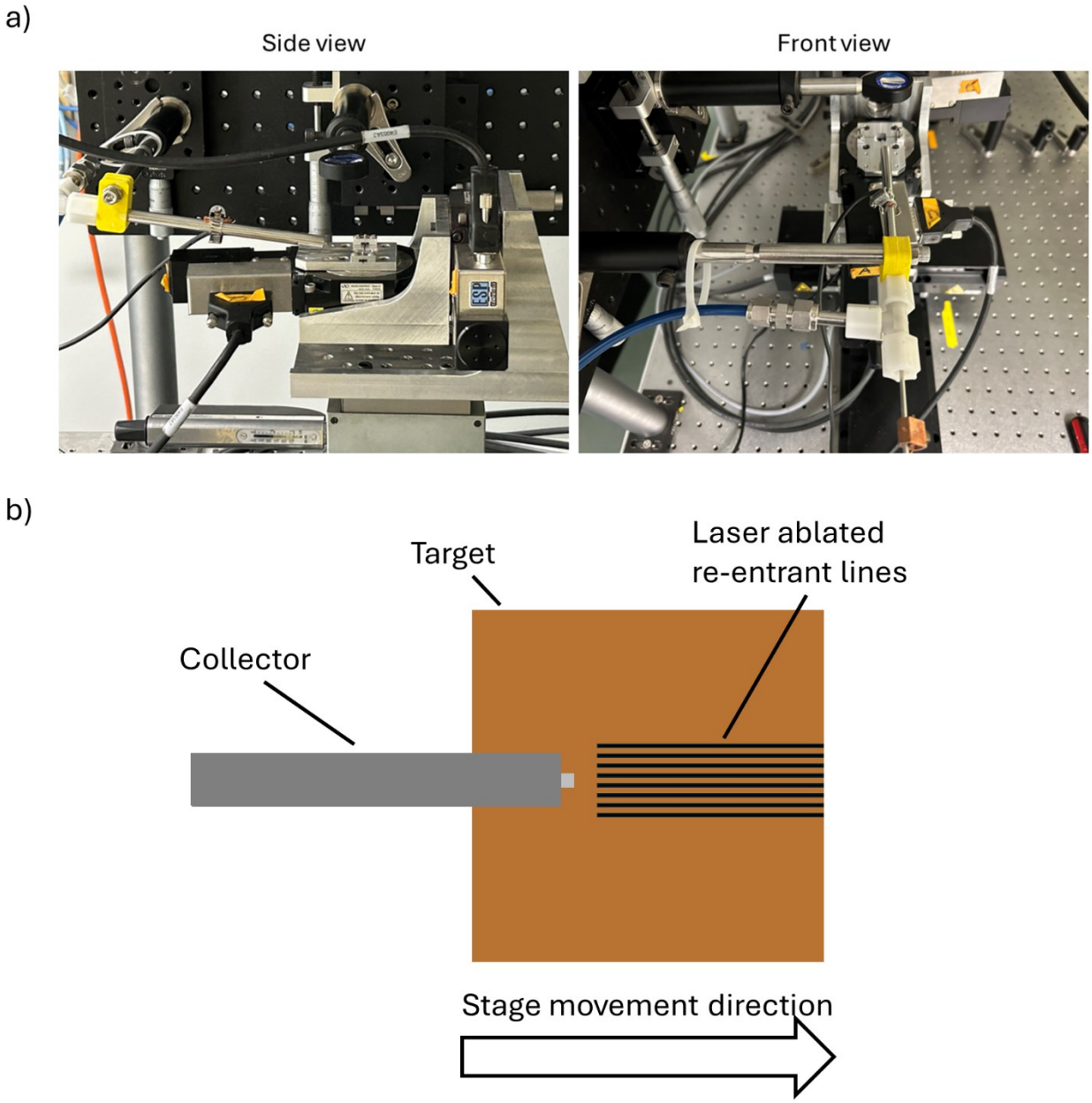

Figure 10: Positioning of nanoparticle collector relative to a) 5-axis stages and mounting breadboard and b) laser ablated re-entrant lines

Using copper as the target material, the re-entrant structures were generated with an industrial turnkey femtosecond laser (Light Conversion Carbide). The laser machining settings that were used are shown in Table 8.

Table 8: Laser settings used for machining on 5-axis stages

Parameter	Value
Pulse duration [fs]	224
Wavelength [nm]	1030
Fluence [J/cm^2]	37.4
Frequency [kHz]	10
Pulse overlap [%]	96.5
PPS	28.9
Lens focal length [mm]	50
Number of overscans	10

Although these experiments used a considerably higher fluence than the experiments done using the Coherent Libra laser system, conclusions can still be made on the effectiveness of the collector when compared to a control re-entrant structure where no nanoparticle removal mechanism was used.

4.9. Nanoparticle plume videography

Nanoparticle plume videography was done using high speed imaging (Photron Fastcam Mini AX200) as outlined in the work of Paolasini and Kietzig [87]. By using a frame rate that was close to (but not equal to) the laser pulse frequency, the camera and laser were synchronized at a given interval. The difference in the frequency of the camera and laser causes a time delay, Δt, between the camera capturing frames and the laser pulsing. This time delay increases with each subsequent frame capture as depicted in Figure 11. The first frame captures the initial instance of plume expansion. The second frame captures the next pulse's plume at a later stage of expansion than the first pulse's plume since it is delayed by Δt. The third frame captures the plume of again the next pulse (third pulse in this example series) at a later expansion stage than the first two plumes since it is delayed by $2 \cdot \Delta t$, and so on. This technique is very useful for time resolved plume expansion imaging granted that the laser and camera frequencies are constant, and that each plume can be treated as identical.

Considering the laser and camera frequencies, a time delay of 43 ns was calculated. This defines the effective frame rate where successive frames of plume expansion are temporally separated by 43 ns.

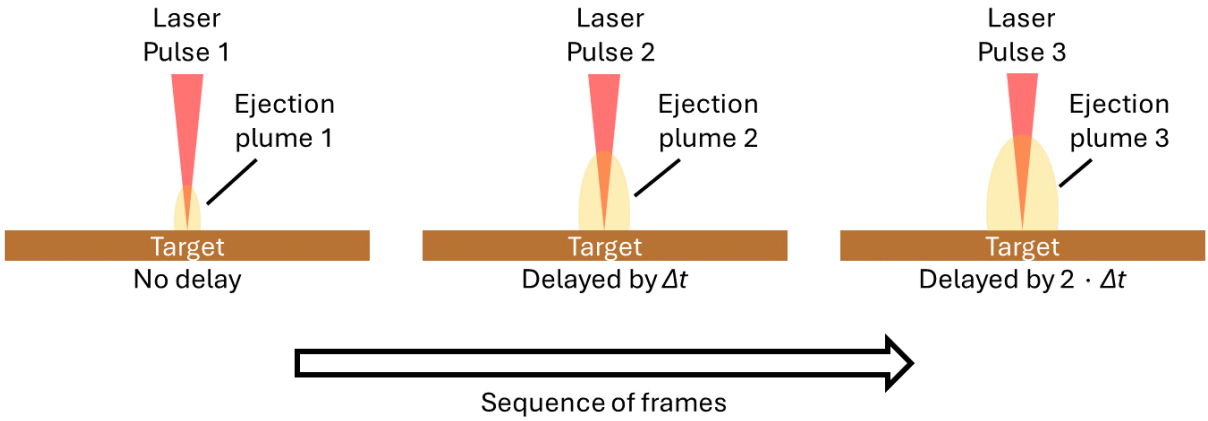

Figure 11: Schematic depicting time delay and sequence of frames

4.10. Nanoparticle in-flight functionalization

To test a methodology for in-flight functionalization, a capacitively coupled – dielectric barrier discharge plasma reactor was assembled as shown in Figure 12.

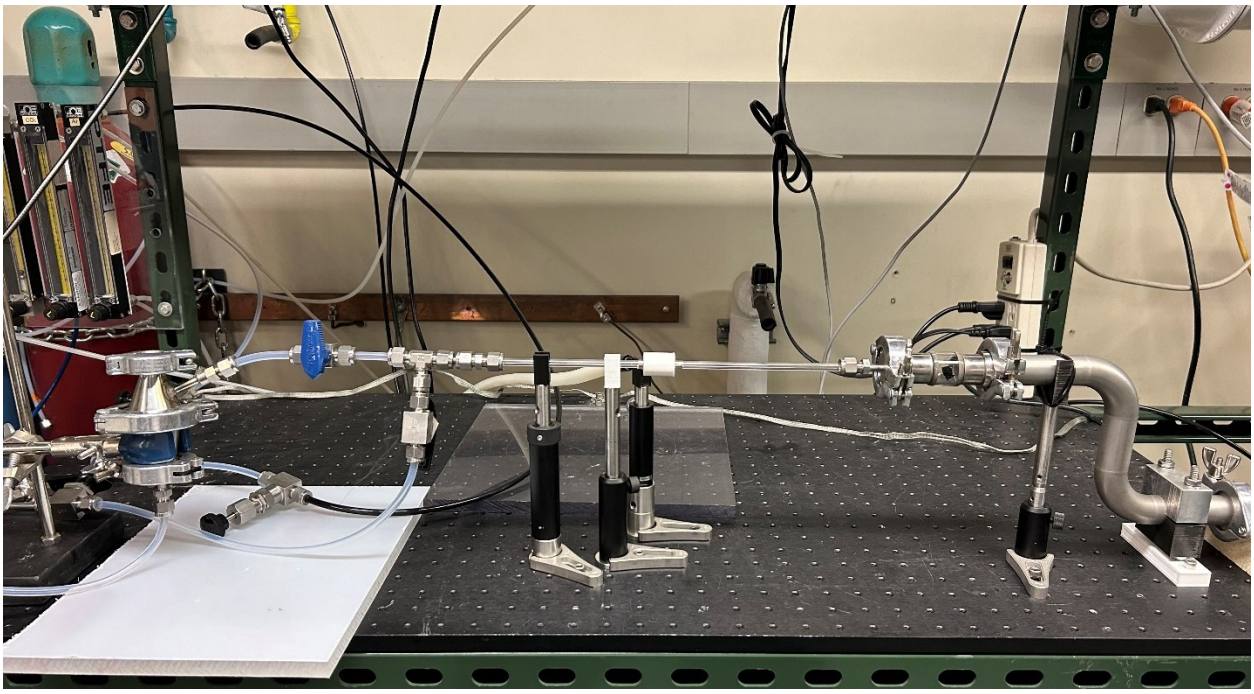

Figure 12: Capacitively coupled - dielectric barrier discharge plasma reactor for in-flight functionalization

The reactor can be divided into two main components: the discharge area (right hand side) and the powder feeder (left hand side). The discharge area, shown in Figure 13, contained a high-voltage and ground electrodes separated by 7 inches (17.8 cm) in a ring-coupled configuration around a quartz tube with an outer diameter of ¼ inches (0.64 cm). Connected to the right of the quartz tube is the collection chamber (10.2 cm in length and 2.5 cm in diameter) containing silica wool to trap the nanoparticles. To the left of the discharge area, a union tee was connected to merge the powder feeder and by-pass gas lines. The ground electrode was connected to earth ground by braided ground wiring. The high voltage electrode was connected to a high-voltage amplifier (Trek model 20/20C). The amplifier was fed a signal from a function generator (Siglent SDG 1032X) that was amplified by a factor of 2000.

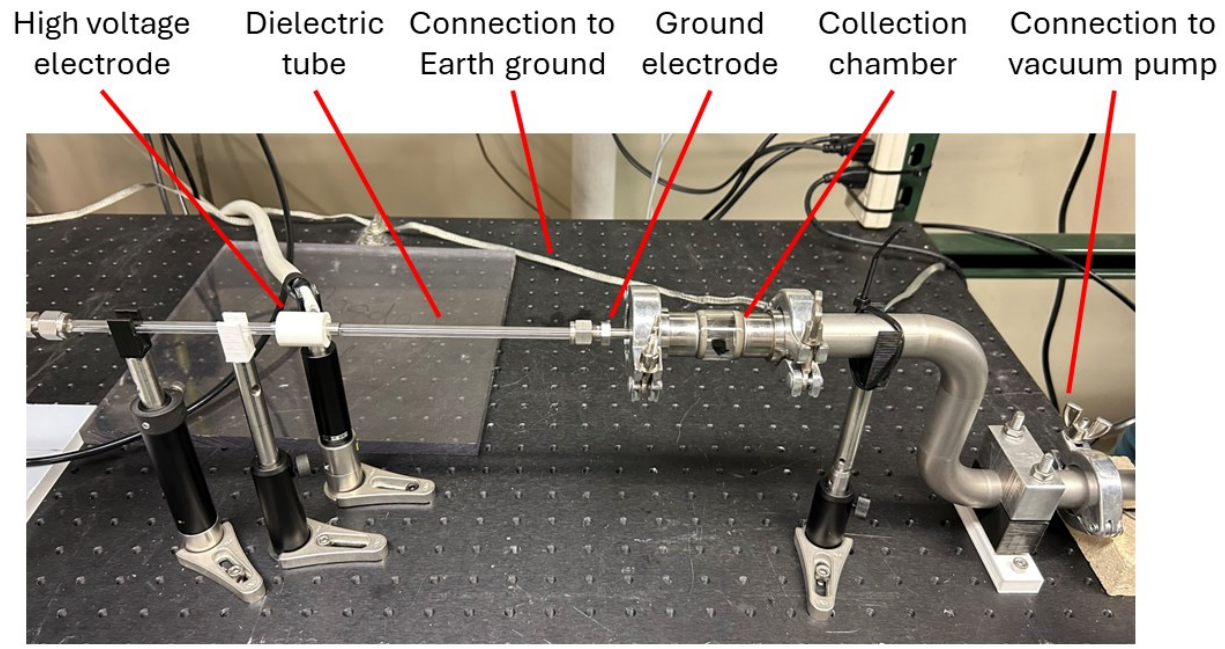

Figure 13: Discharge area of plasma reactor with labels

The powder feeder, shown in Figure 14, was mounted on the table using a post and a clamp. The red arrows indicate the direction of gas flow in the by-pass line. The by-pass line was used to generate a stable plasma before the powder was injected. The blue arrows indicate the direction of gas flow from the powder feeder towards the discharge area. The gas flow was injected from the bottom of the chamber so that the bulk gas movement would direct the powder into the plasma. The upward movement of the powder was meant to emulate the ejection of nanoparticles from the ablation point during laser micromachining.

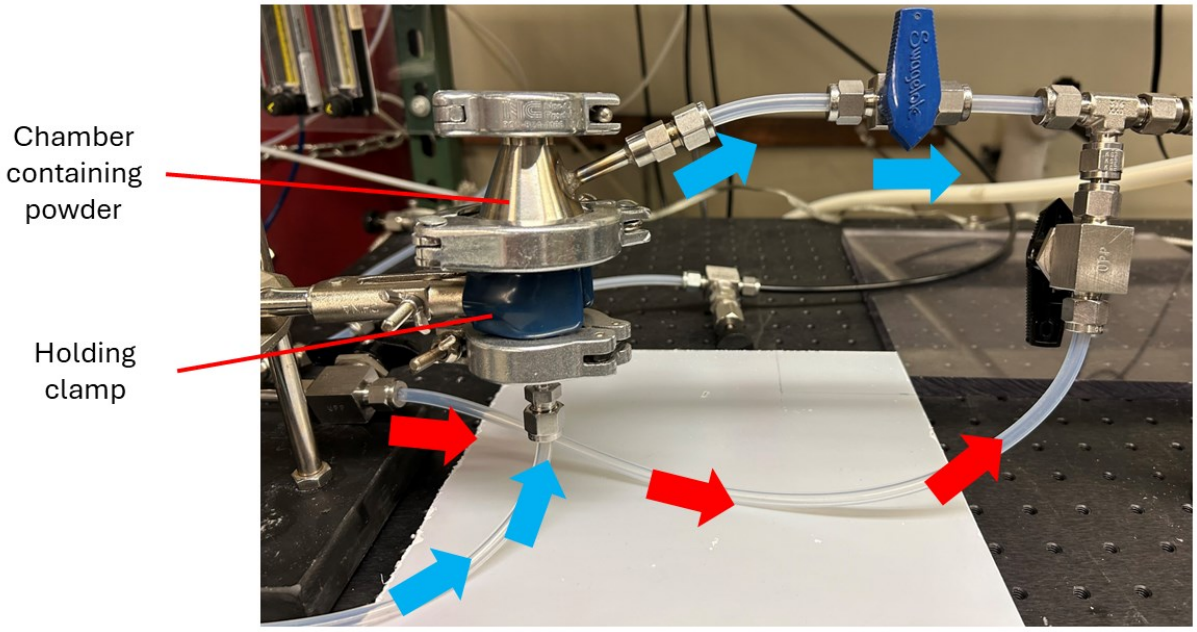

Figure 14: Powder feeder with labels and arrows depicting direction of gas flow

Initially, the copper oxide powder was loaded into the powder chamber. The chamber was then connected to the gas line leading to the discharge area. To generate a stable plasma, the valves on the inlet and outlet lines of the powder chamber remained closed while gas flow to the discharge area was permitted by the by-pass line. Once the plasma was generated, the valves around the powder chamber were opened allowing for the injection of the copper oxide nanoparticles. Figure 15 shows the plasma reactor with a stable discharge inside the quartz tube.

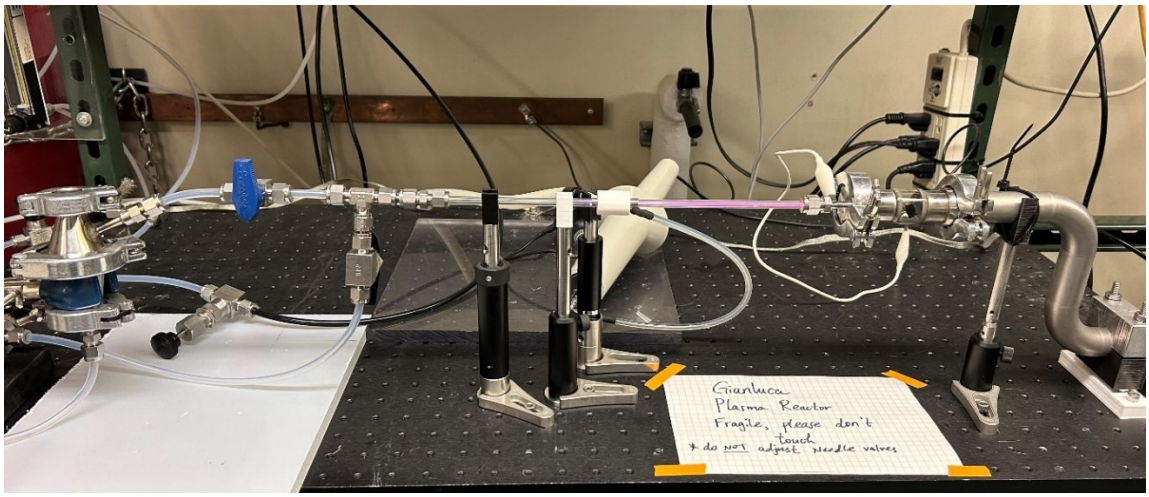

Figure 15: Reactor with plasma discharge inside quartz tube

Two different trials for in-flight functionalization and one control experiment were performed. For the control experiment, only argon was injected into the reactor. For the in-flight functionalization trials, a mix of argon and ethane was injected. The plasma reactor operating parameters for each trial are shown in Table 9. The difference between the two in-flight functionalization trials was the magnitude of the applied potential to the high voltage electrode.

Table 9: Summary of settings used for testing in-flight functionalization methodology

Trial no.	**Applied alternating potential [kV_{p-p}]**	**Frequency [kHz]**	**Pressure [Torr]**	**Gas cylinder delivery pressure [psi]**	**Ar:C_2H_6 flow rate ratio [sscm:sccm]**	**Duration [minutes]**
Control	10.0	15	4	15	2000:0	5
1	10.0	15	4	15	2000:20	5
2	15.0	15	4	15	2000:20	5

5. Results and Discussion

5.1. Determination of optimized nanoparticle collection process parameters

The parameters investigated in these experiments were the machining stage velocity and the suction flow rate. Table 10 displays the range of settings selected for experimentation based on preliminary trials.

Table 10: Parameters considered in determination of optimal collection settings

Parameter	Low setting	Intermediate setting	High setting
Stage velocity [mm/s]	1	5	10
Suction flow rate [m^3/h]	0	0.57	1.14

The effect of the suction flow rate is shown in Figure 16 a). Based on these results, it is evident that there was an optimal suction flow rate close to 0.57 m^3/h. To confirm this finding, a fine tuning of the suction flow rate was performed using a stage velocity of 5 mm/s, as shown in Figure 16 b).

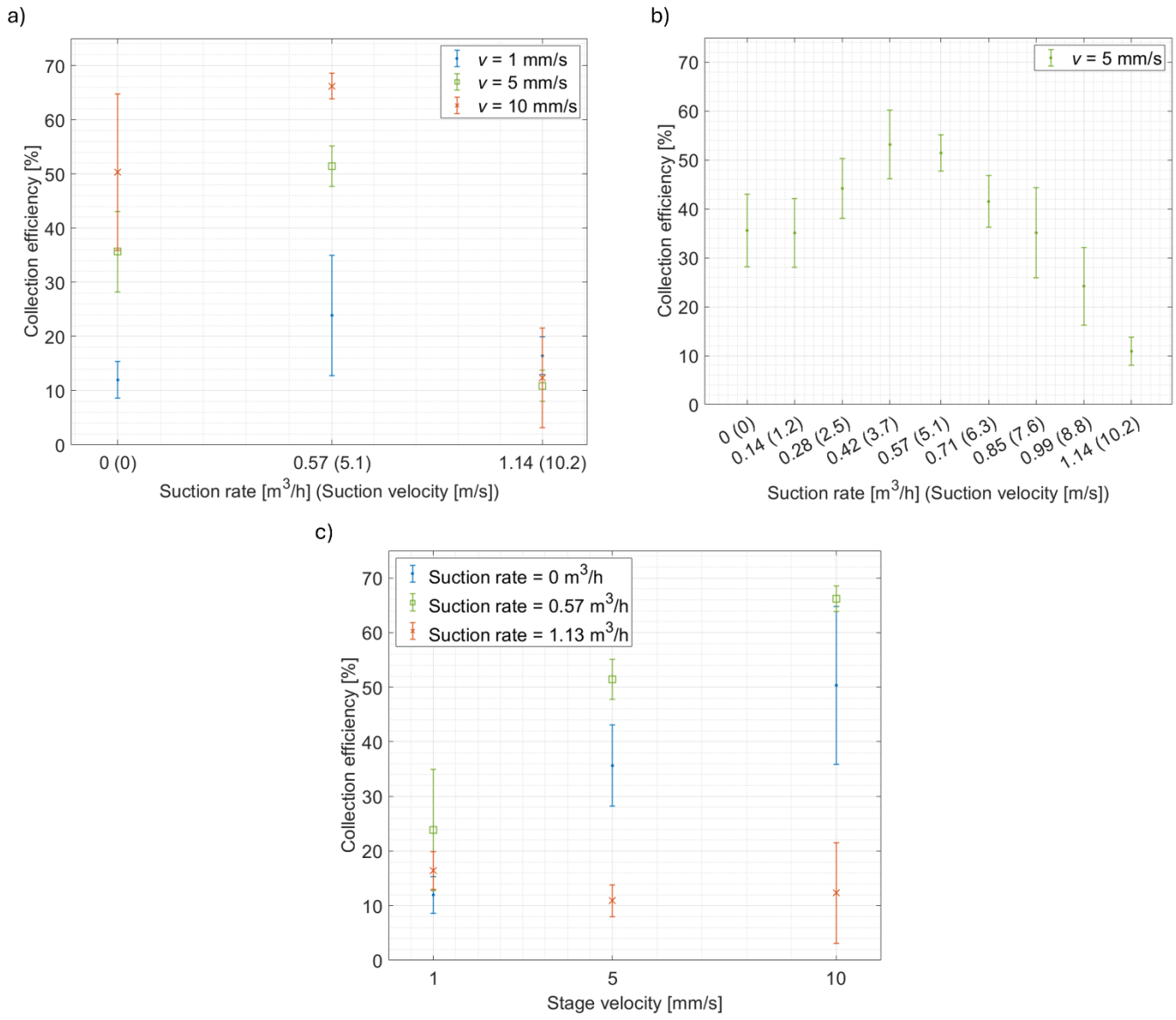

Figure 16: Effect of a) suction flow rate, b) fine tuned suction flow rate, and c) stage velocity on collection efficiency (values in brackets represent suction gas velocity in m/s).

The fine tuning of the suction flow rate confirms an optimal suction rate that was close to 0.57 m^3/h. This finding indicates that a balance must be met between attracting the ejected material towards the collector electrode without executing too much suction for there not to be any collection at all. On the higher end of the suction flow rate range, the collection efficiency was at its lowest. This is attributed to the increased suction force causing ejected material to be drawn past the collector electrode and down the suction line. On the lower end of the suction flow rate range, there was some collection, however, most of the ejected material was lost to the environment since the suction force was weaker. When comparing the suction gas velocity to the expected

plume expansion velocity (~ 10 m/s), it was evident that using a suction velocity close to half of the expansion velocity led to optimal collection.

Taking a different perspective on these results, the effect of the stage velocity is shown in Figure 16 c). The results indicate that for a fixed suction rate, the higher stage velocity led to higher collection efficiency. However, this finding was not observed for the experiments done using a suction rate of 1.13 m^3/h, as it was too high to draw any meaningful conclusions on the effect of the suction rate (i.e., regardless of stage velocity, almost all the material was being drawn down the suction line). The enhanced collection is attributed to the reduced interactions between incoming laser pulses and the expanding ejection plume at higher stage velocities. This idea is more easily explained by considering the extreme cases of very high and low stage velocity as shown in Figure 17.

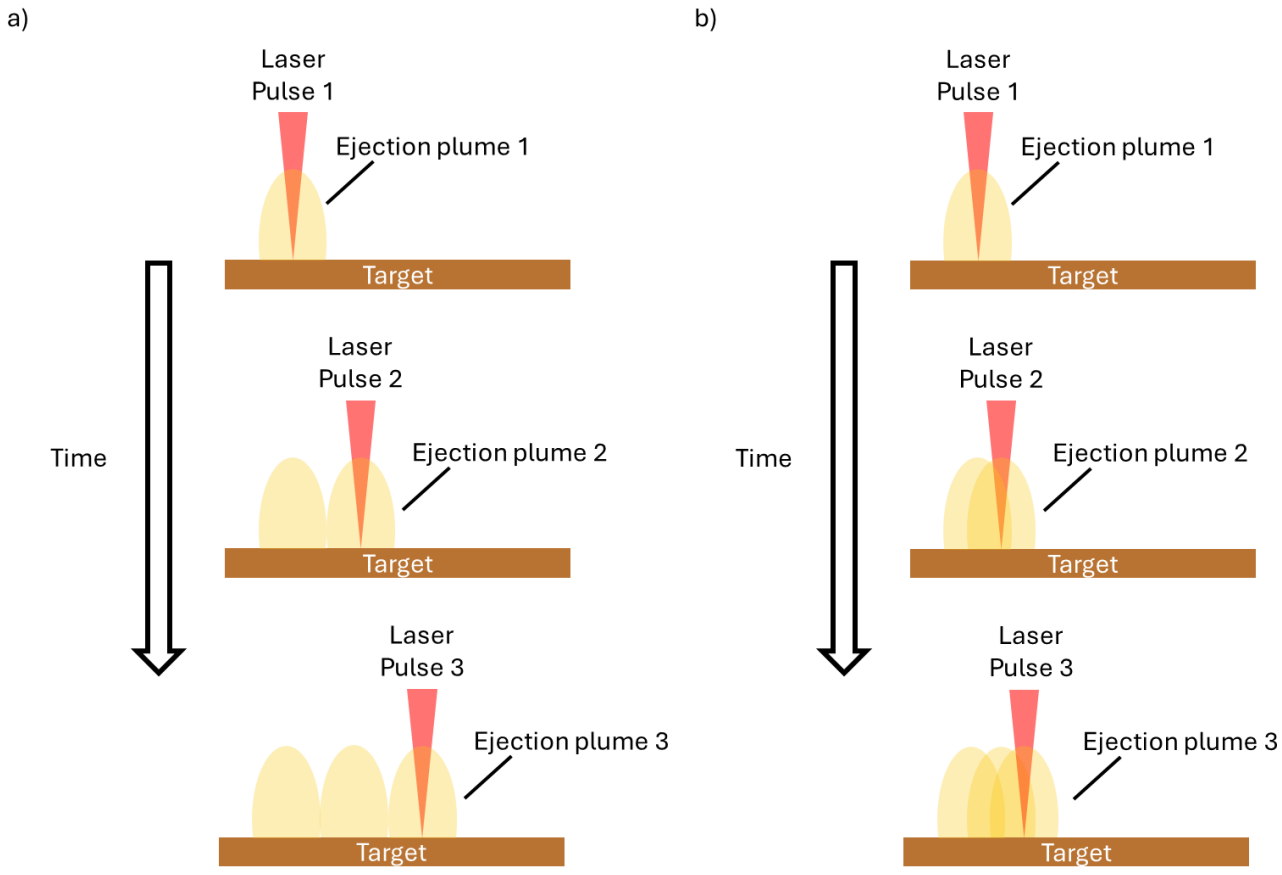

Figure 17: Laser pulse and ejection plume interaction for a) high stage velocity and b) low stage velocity

The degree of laser beam interaction with expanding ejection plumes influenced the amount of material redeposited on the surface. For the high stage velocity case depicted in Figure 17 a), the PPS is low (i.e., there is increased distance between irradiated laser spots from subsequent pulses). This means that there is less overlap between a laser pulse and the prior ejection plume generated from a previous laser pulse. The opposite is true for the low velocity case depicted in Figure 17 b) where the PPS is high and there is more overlap between a laser pulse and the prior ejection plume. Due to the increased interaction between the laser beam and expanding material for the low stage velocity, more material is pushed back towards the target surface by momentum transfer between the ejected material and incoming laser pulse. Since more material is pushed towards the surface, away from the collector, the collection efficiency was low. On the other hand, for the high stage velocity case, less material is pushed back to the surface causing the collection efficiency to be higher.

Based on this result, it is evident that laser machining at low PPS setting is optimal for nanoparticle collection. For more advanced laser systems, the frequency of laser pulses can be decreased such that the PPS decreases. For laser systems with a fixed frequency, the only way to decrease the PPS is to increase the machining velocity (granted a fixed fluence is being used). However, for the generation of certain surface structures, a high PPS is required to ensure ample material removal from the surface. One could simply increase the fluence to achieve more material removal, but that is not always possible or convenient. Therefore, this becomes a question of how laser machining trajectories can be adjusted to increase the space between sequential material ejection plumes, while still obtaining the desired surface structure. One option is to re-arrange how laser ablated lines are generated on the surface. To illustrate this, consider the traditional method in which a line is ablated on a surface as depicted in Figure 18 a).

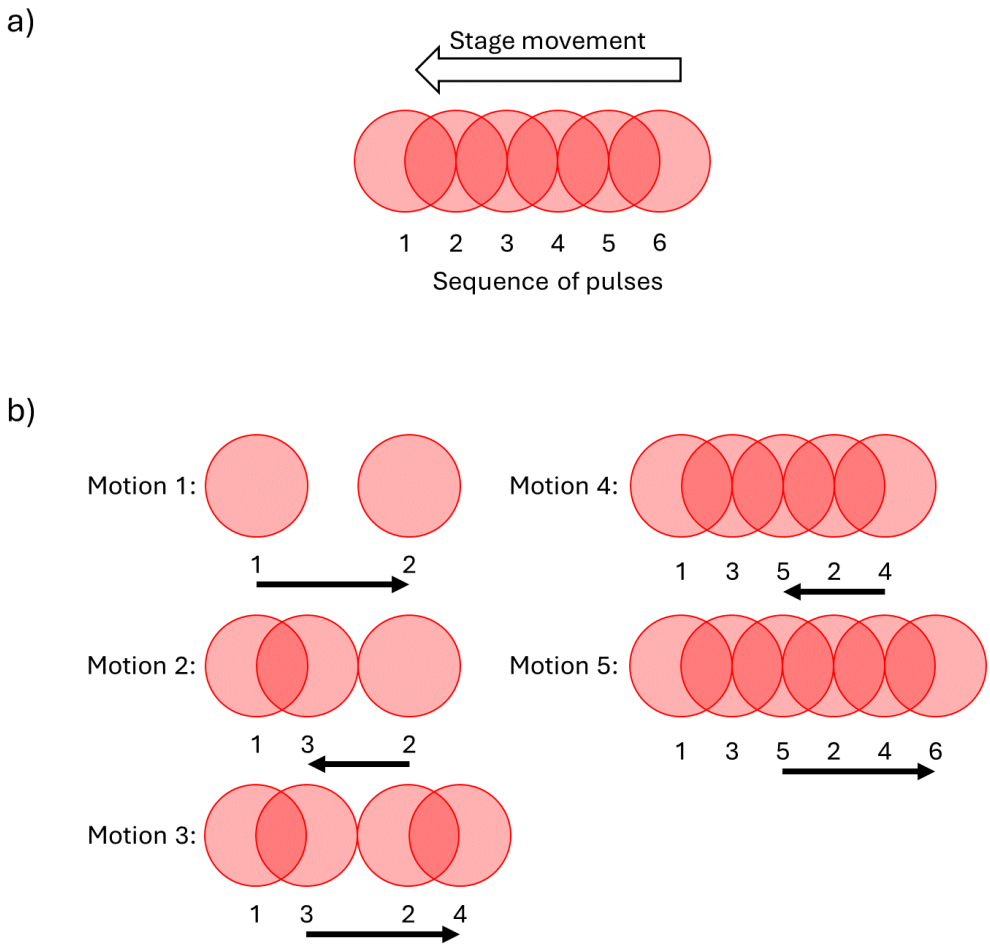

Figure 18: Laser ablated line generated from stage movement in a) one direction and b) back and forth motion (with black arrows indicating stage motion)

This technique is simple in that the laser machining stage moves in a single direction. Yet, it is possible to change the way the laser machining stages move such that there is more space between each subsequent pulse of the laser. This idea is shown in Figure 18 b), where the stage moves in a series of back-and-forth motions to generate the same laser ablated line depicted in Figure 18 a). Although this method of laser machining is convenient for nanoparticle collection, it is notably more time consuming due to the alternating stage motion. Additionally, there is complexity to such a technique when intricate surface structures are to be generated. Table 11 shows a qualitative analysis of the two ablation techniques discussed above.

Table 11: Comparison of ablation line generation techniques

Line generation technique	Time requirement for 2 × 2 mm^2 patch at 1 mm/s stage speed	Complexity	Distance between subsequent laser pulses
Single direction stage movement	6 minutes	Low	Low
Alternating stage movement	70 hours	High	High

It is worth noting that in industrial settings, where galvanometer scanners are predominantly used (rather than translational stages), the time consumption of the alternating stage movement technique can be dramatically reduced.

5.1.1. Comparison between NP collector and in-line HEPA filter

The performance of the nanoparticle collector was compared to that of an in-line HEPA filter that has similar performance in trapping efficiency to HEPA filters that are used in industry. Using the optimal suction flow rate of 0.57 m^3/h and optimal stage velocity of 10 mm/s, the trapping of nanoparticles in the filter is compared to the material recovery using the collector as depicted in Figure 19.

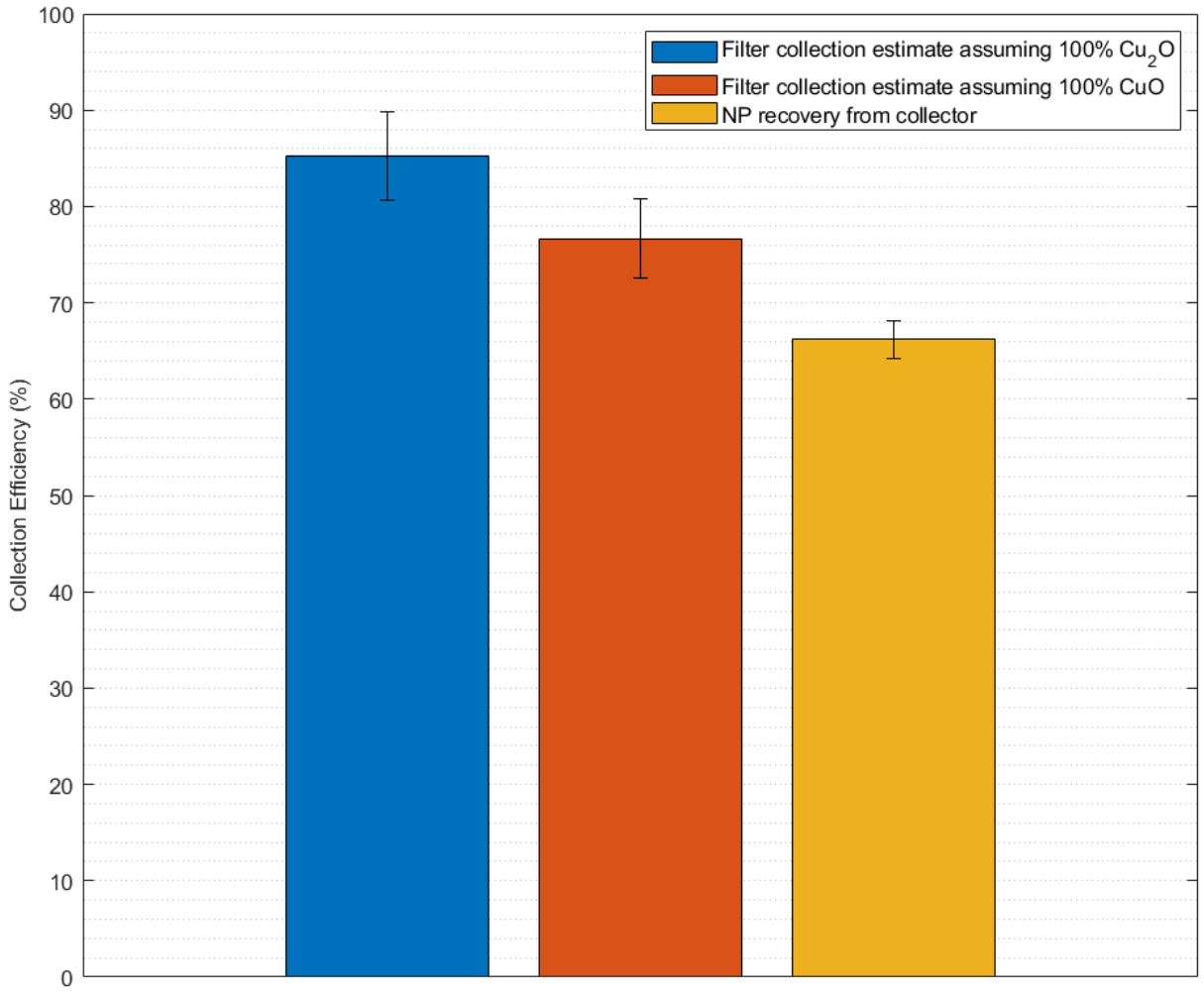

Figure 19: Comparison between the performance of the in-line HEPA filter and the nanoparticle collector

These results indicate that the filter was more efficient in collecting material when compared to the recovery from the collector. However, it is important to point out that removing the collected material from the filter is very difficult. Methods to remove trapped material such as sonication, vacuum washing, water/solvent washing, and blowing with dried air can be energy and resource intensive [88]. Contrarily, the material recovered using the collector is readily accessible for further use.

5.1.2. Assessment of the collector's performance for re-entrant structures

The collector was operated using the optimal suction flow rate, 0.57 m^3/h, and stage velocity, 10 mm/s. Figure 20 shows a side view of the structures clearly indicating the impact of the nanoparticle collection (the blue dotted lines represent the expected profile).

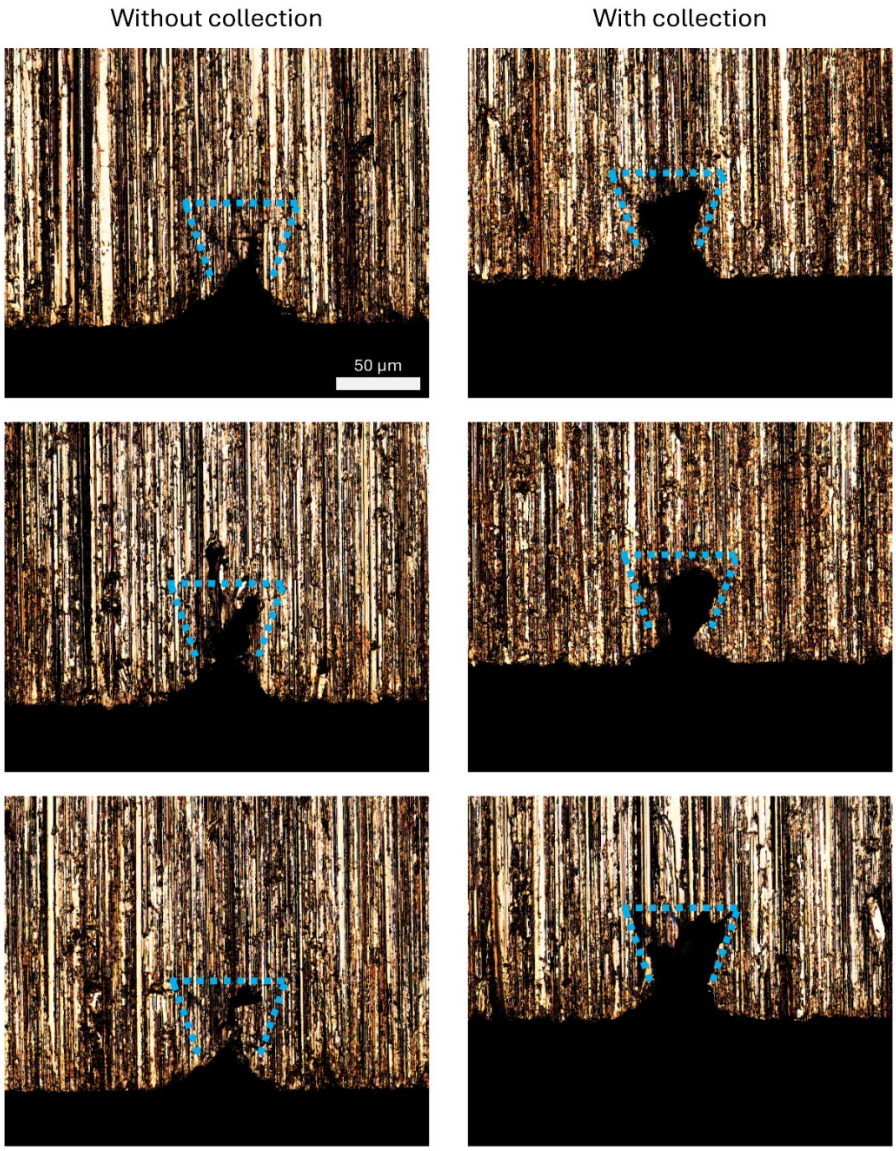

Figure 20: Confocal image of side view of re-entrant structures generated with and without nanoparticle collection (scale bar in top left image applies to all images)

Figure 21 shows SEM images comparing the top view of the re-entrant structures generated with and without nanoparticle collection. On the right edge of the structure, there is less nanoparticle redeposition on the surfaces for samples produced using nanoparticle collection. On the interior of

the structure, there was slightly less nanoparticle accumulation when collection was used, however, the disparity was not clear from the top view.

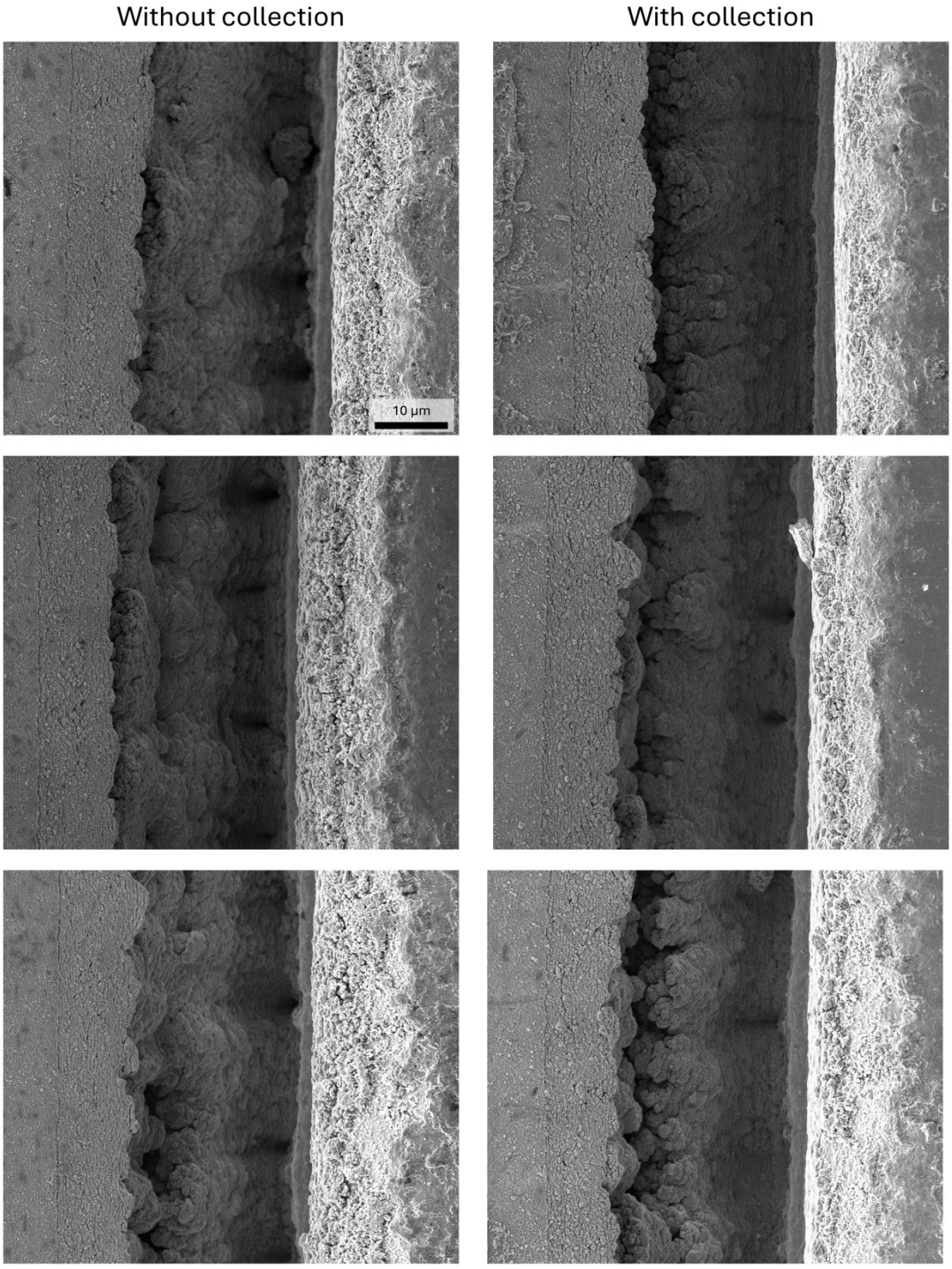

Figure 21: SEM images of top view of re-entrant structures generated with and without nanoparticle collection (scale bar in the top left image applies to all images)

Based on the side view, the nanoparticle collection assisted in generating a more well-defined re-entrant structure. The collection evidently removed much of the material that would normally become trapped inside the pore. However, the removal of the ejected material from the pore was not perfect due to physical limitations of laser machining re-entrant structures. Additionally, due to spatial constraints of the 5-axis stages the collector was oriented in parallel with the laser ablated lines which is not optimal for collection (i.e., collection is most efficient when the collector is perpendicular to the laser ablated lines) [3]. Considering the pore size, there was a high likeliness that ejected material interacted with the overhanging walls causing it to become trapped. Furthermore, through momentum transfer with the incoming laser pulses, trapped nanoparticles were pushed deeper into the pore reducing the likeliness of them being removed. The material removal from the pore could possibly be improved by determining the optimal collector operating parameters for use with the 5-axis stage setup and using the optimal collector orientation. Despite these improvements, it is still likely that there will be some degree of redeposited material within the pore.

5.2. Effect of fluence on nanoparticle collection efficiency

Using the optimal stage velocity and suction flow rate, nanoparticle collection was performed for fluences of 3.0, 4.5, 6.0, and 7.5-times F_{th}. Figure 22 shows the effect of laser fluence on nanoparticle collection efficiency.

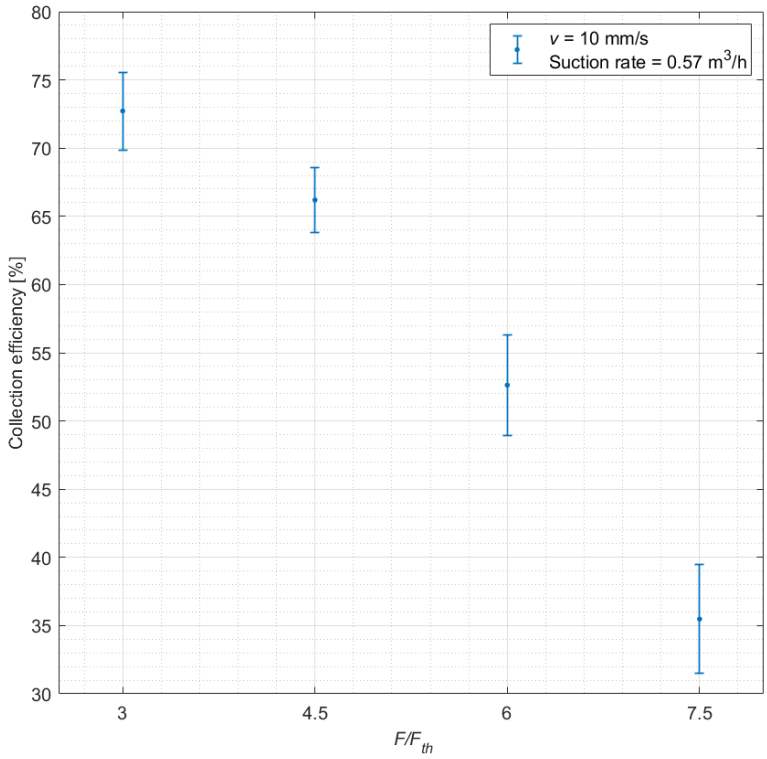

Figure 22: Effect of laser fluence on collection efficiency

Evidently, material ablated at a lower fluence resulted in more efficient material recovery. The explanation behind this finding is the fluence dependent dynamics of nanoparticle plume expansion during laser ablation. This explanation was verified by analyzing redeposited nanoparticles on the target surface as depicted in Figure 23.

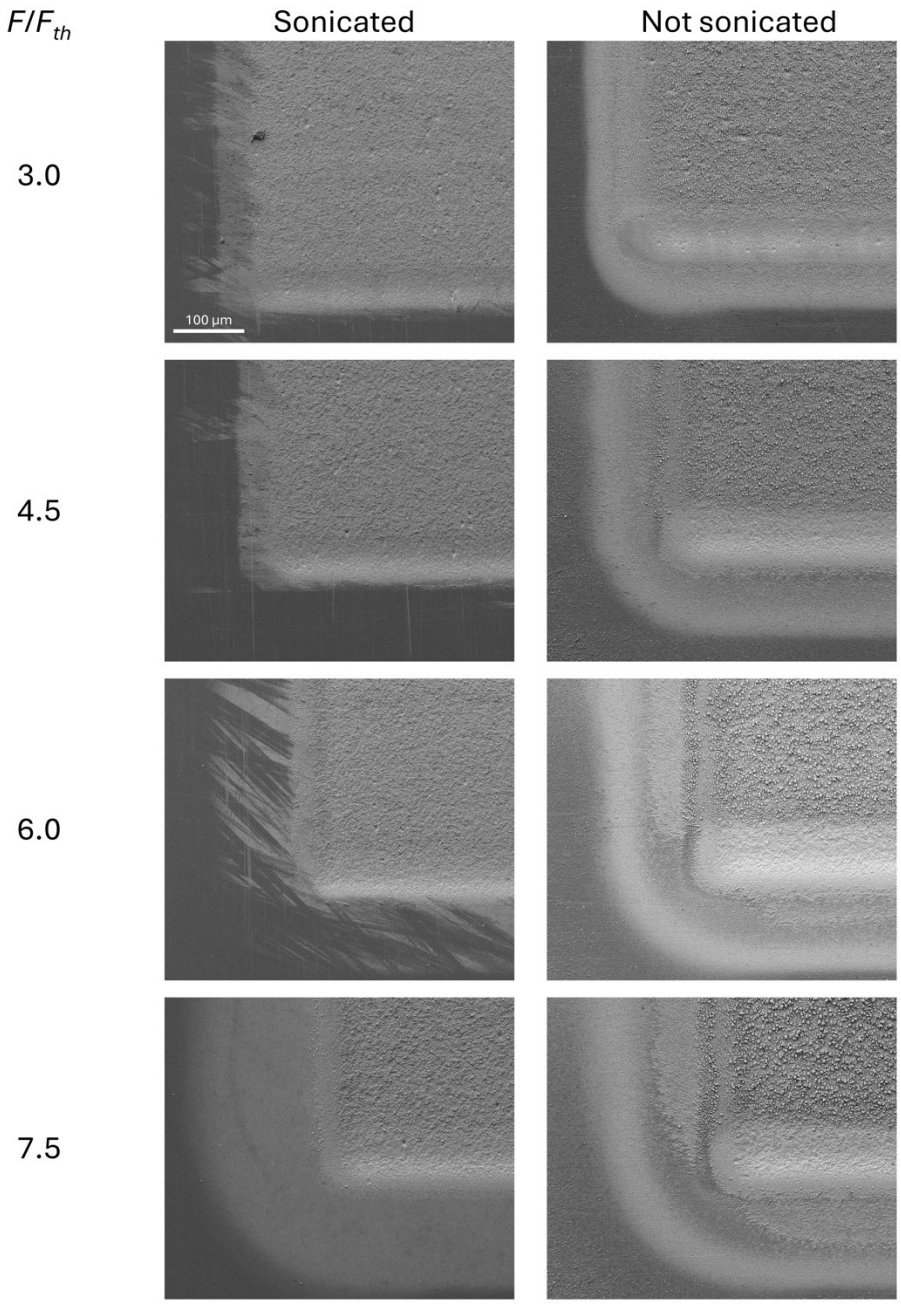

Figure 23: Redeposited nanoparticles on target sample surfaces for varying laser fluences (scale bar in the top left applies to all images)

For comparison, samples were also sonicated to more clearly see the shape of the laser ablated raster scan patch. The SEM images of Figure 23 indicate that the film of redeposited nanoparticles expands further from the laser irradiated area for samples ablated at higher fluences. Therefore, since the ejection of material is more confined at a lower fluence, the collection is more efficient.

To further support the claim that fluence-dependent nanoparticle plume expansion dynamics affects collection efficiency, high-speed plume imaging was performed. Figure 24 depicts plume expansion for both low and high fluence settings (the slight angle in the images of the ejected material plumes was likely caused by advective air flow in the temperature and humidity-controlled laser chamber).

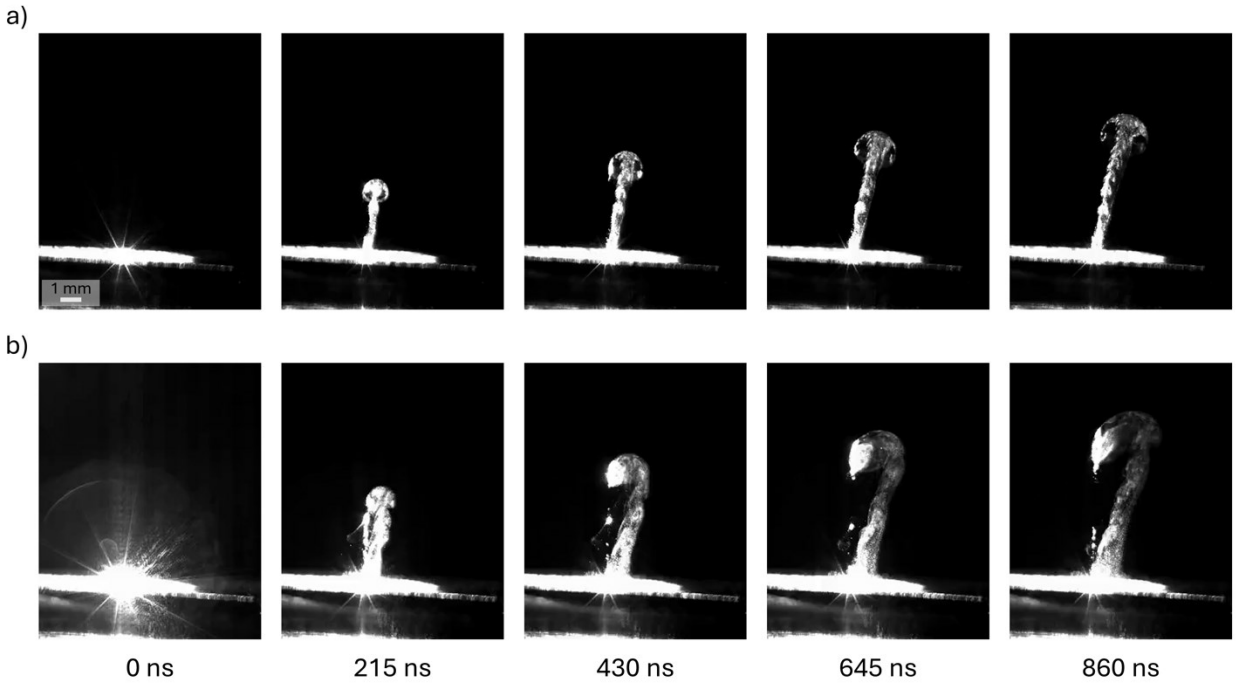

Figure 24: Time-resolved high-speed images of plume expansion for fluences of a) 3.0 and b) 7.5 times F_{th} (scale bar in the top left image applies to all images).

Based on these images, it was concluded that for the sample ablated with a higher fluence, the ejection plume is larger, and it expanded faster. To confirm this, the vertical and horizontal position of the expansion plume for selected frames were analyzed to obtain a position profile of the plume as depicted in Figure 25.

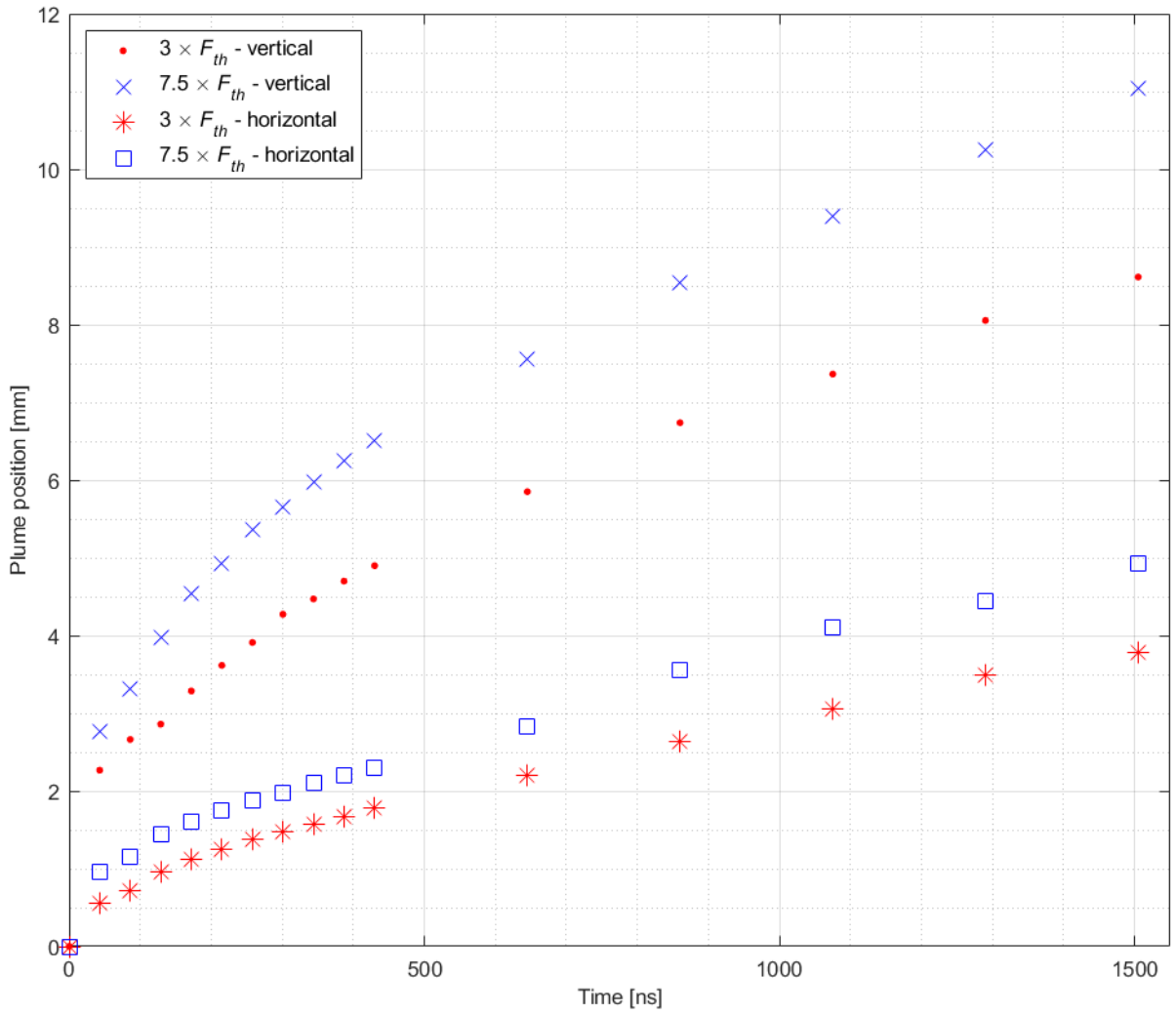

Figure 25: Vertical and horizontal position of ejection plumes for low and high fluence settings

Although the expansion velocity for each of the plumes was not constant (in either direction), at any point during the expansion, the plume generated at higher fluence expanded faster. Since the higher fluence plume expanded faster, the material was ejected with more kinetic energy than for the lower fluence case. The increased kinetic energy of the nanoparticles allowed for them to expand further in both the radial and axial directions before they started becoming attracted towards the collector. This conclusion is supported by further high-speed imaging analysis with the nanoparticle collector included as depicted in Figure 26.

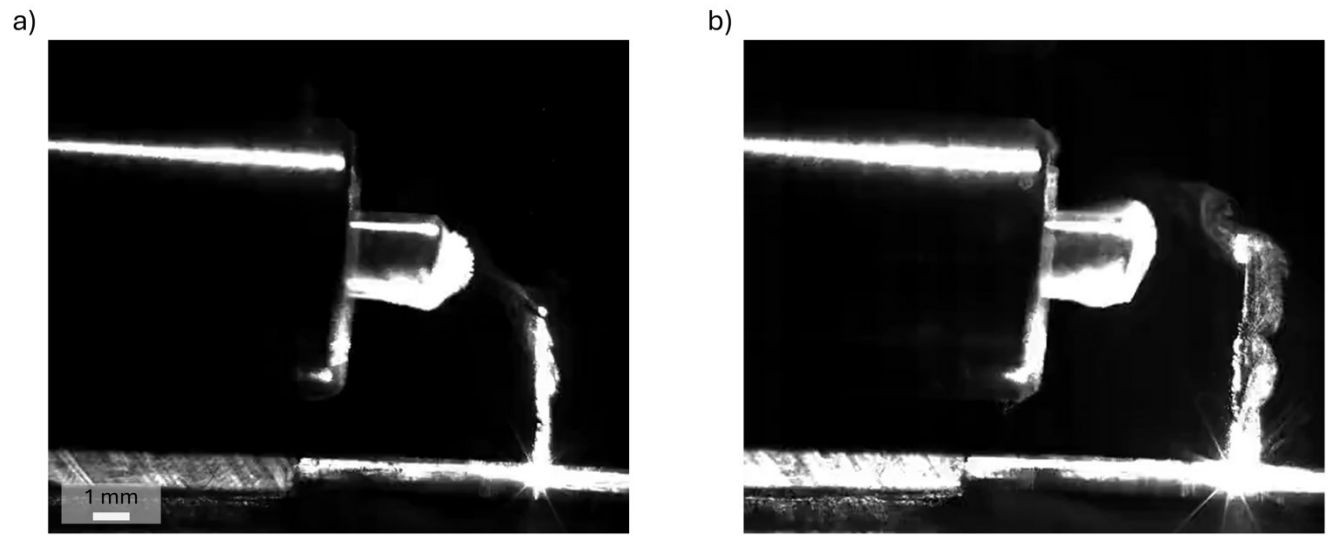

Figure 26: High-speed images of ejection plume with nanoparticle collector for fluences of a) 3.0 and b) 7.5 times F_{th}

The images above clearly indicate that the material ejected using a higher fluence experienced more expansion before being attracted to the collector. On the other hand, the material ejected at the lower fluence is more confined since less expansion occurred before nanoparticles were drawn towards the collector. Therefore, the ejected material took a more direct path to the collector at the lower fluence setting leading to an increased collection efficiency. However, it is possible that by increasing the vertical height of the collector above the target, the collection efficiency at the higher fluence setting could be improved.

In the context of laser machining, there is a common question of using a high fluence with few overscans or low fluence with many overscans to achieve a certain depth for surface structures. More precisely, a desired total accumulated fluence (given by Equation 5) can be achieved using different machining strategies. If a high fluence is used, individual laser pulses can be summed across a laser ablated area to achieve some total accumulated fluence. This same accumulated fluence can be achieved by using lower fluence pulses that are overscanned on top of each other across the same laser ablated area. Based on the results obtained with this collector configuration, using many overscans at a low fluence would lead to optimal material recovery. The issue that arises with this scenario is that laser machining many overscans can take a long time. This can become inconvenient in cases where large areas are being laser machined. Although the collector settings used were not optimal for collection with high fluence machining, it is possible to tune

collector settings for this application. For example, a higher suction rate and/or higher applied potential to the collector electrode would be an effective way to attract the more dynamic nanoparticle plume produced by higher fluence machining. Therefore, this becomes a question of collector design and optimization rather than a question of what fluence setting to use. To account for the increased material removal and plume expansion at higher fluences, the size of the collector can be made larger. The collector can also be positioned further away from the target material so that collection can occur at a point where the plume expands more slowly. In general, nanoparticle collectors should be designed with an idea of the fluence dependent plume dynamics.

5.3. Effect of target material composition on collection efficiency

To investigate the effect of target material composition on collection efficiency, the process settings displayed in Table 12 were used. These settings were chosen to ensure ample material collection for analysis of the different components of each alloy.

Table 12: Process settings used for collection experiments with alloys

Parameter	Value
Stage velocity [mm/s]	1
Suction flow rate [m^3/h]	0.57
F/F_{th}	4.5

For each alloy, the components of interest were compared across two criteria that are summarized in Table 13.

Table 13: Summary of criteria used to assess the collection of alloy components

Criteria	Definition
Collection efficiency	The mass of a component in the collected sample relative to how much of that component was laser ablated.
Mass percent in collected sample	The mass percentage of a component in the recovered material from the collector.

5.3.1. Aluminum 6061

For aluminum 6061, the recovery of material was limited to aluminum. The results for this alloy are summarized in Table 14.

Table 14: Summary of results for components in aluminum 6061

Component	Mass percent in non-ablated alloy [%]	Collection efficiency [%]	Mass percent in collected sample [%]
Al	99.8	12.9%	~ 100%
Cr	0.2	~ 0%	~ 0%

The lack of collection of chromium may be attributed to the rather low mass fraction of this component in the alloy. It is also possible that the collection of aluminum was dominant because of its higher electrical conductivity when compared to chromium.

5.3.2. Brass 360

For brass 360, the collection of copper and zinc were compared with the results displayed in Figure 27. These results clearly indicate that copper and zinc were recovered with the same efficiency. This also means the mass fraction in the collected sample was consistent with the pristine alloy.

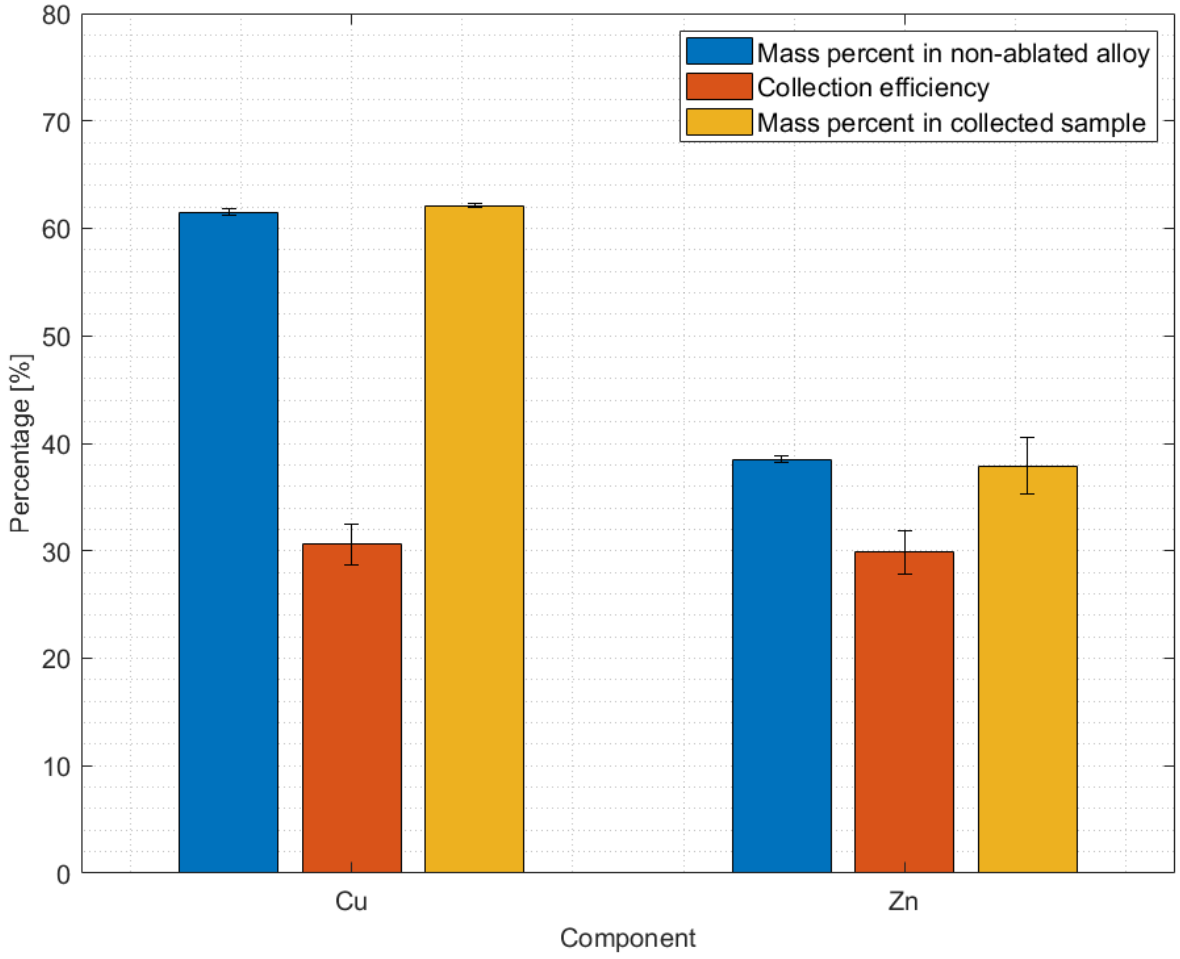

Figure 27: Comparison of recovery of copper and zinc in brass 360

This result is interesting in that copper is almost four times more electrically conductive than zinc, yet they collected at the same efficiency. A possible explanation for this is that when ablation was occurring, the nanoparticles that were being ejected had the same composition as the target alloy material. As shown in previous studies, homogenous brass particles can be generated from laser ablation in both air and water [89]. Therefore, the collection process did not favor one alloy component over the other because they were being collected at the same rate, in the same proportions as the pristine alloy.

5.3.3. Stainless steel 304

For stainless steel 304, the collection of iron, nickel, and chromium were compared with the results displayed in Figure 28.

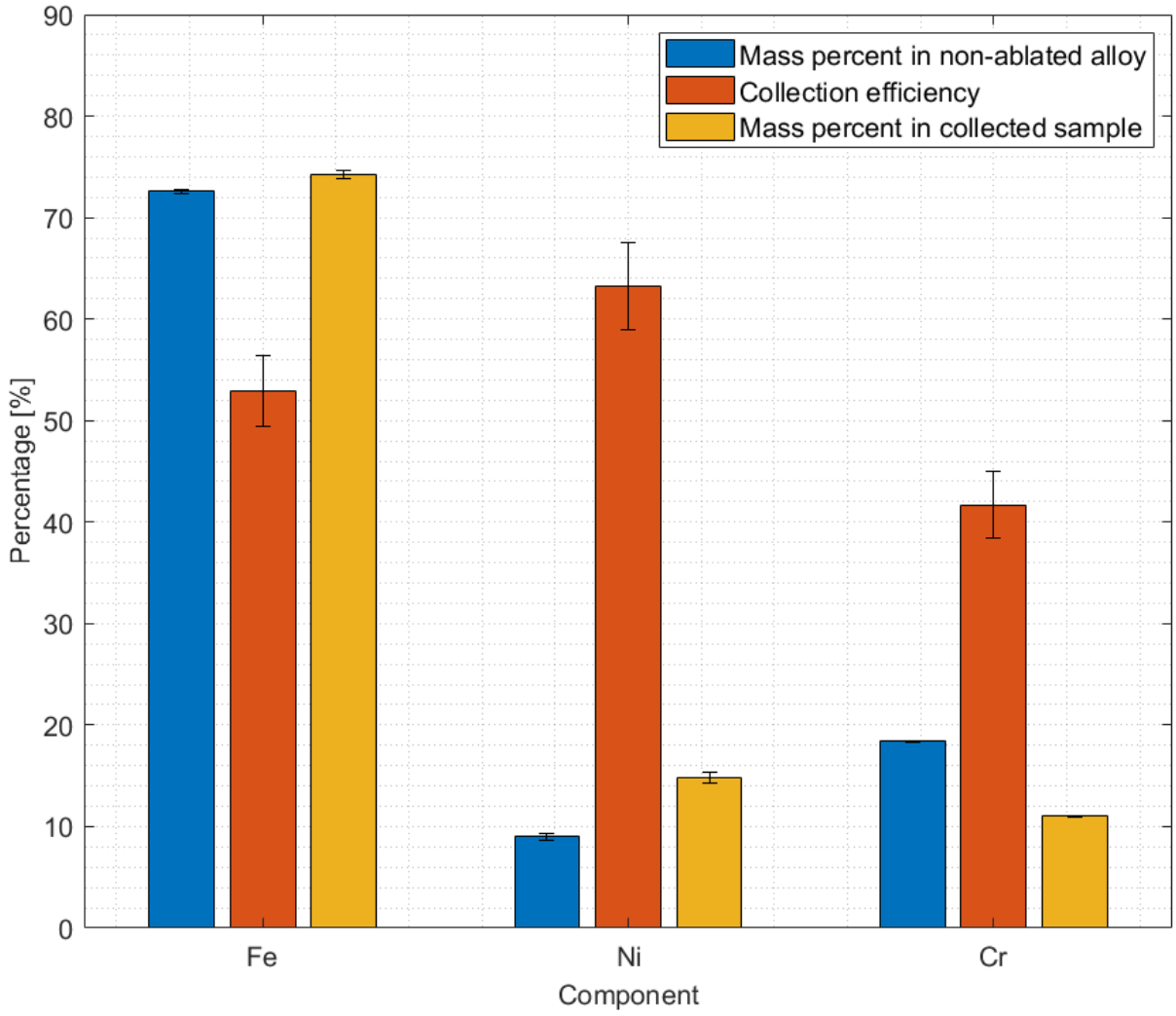

Figure 28: Comparison of recovery of iron, nickel, and chromium in stainless steel 304

Unlike for brass 360, the composition of the pristine stainless steel was different from the recovered material. Although, the composition of the collected material was not drastically different from the alloy. The notable aspect of this result is that the collection efficiency of each component was directly correlated with electrical conductivity (e.g., nickel has the highest electrical conductivity and was collected the most efficiently). This finding can alternatively be explained by considering the effect of grain size relative to the size of the ablation point. For stainless steel 304, the grain size is on the scale of 50 µm [90]. This is slightly larger than the focused laser beam spot size of 40 µm. This means that, at some instances during laser ablation, it is likely that material was ejected which had a different composition from the pristine alloy. This conclusion is further supported by considering the results obtained when ablating brass 360. The

grain size for the brass alloy is on the scale of 10 μm [91]. Therefore, at any point during the ablation of brass, both copper and zinc where being ablated in the same proportions as the pristine alloy since the grain size is smaller than the focused laser beam spot size.

Another key finding related to the collection of stainless steel nanoparticles was their high degree of agglomeration, as shown in Figure 29. Evidently, these particles are clustered together and not individually distinguishable. This finding highlights the necessity for a method to surface stabilize the generated particles which is further discussed in section 5.4.

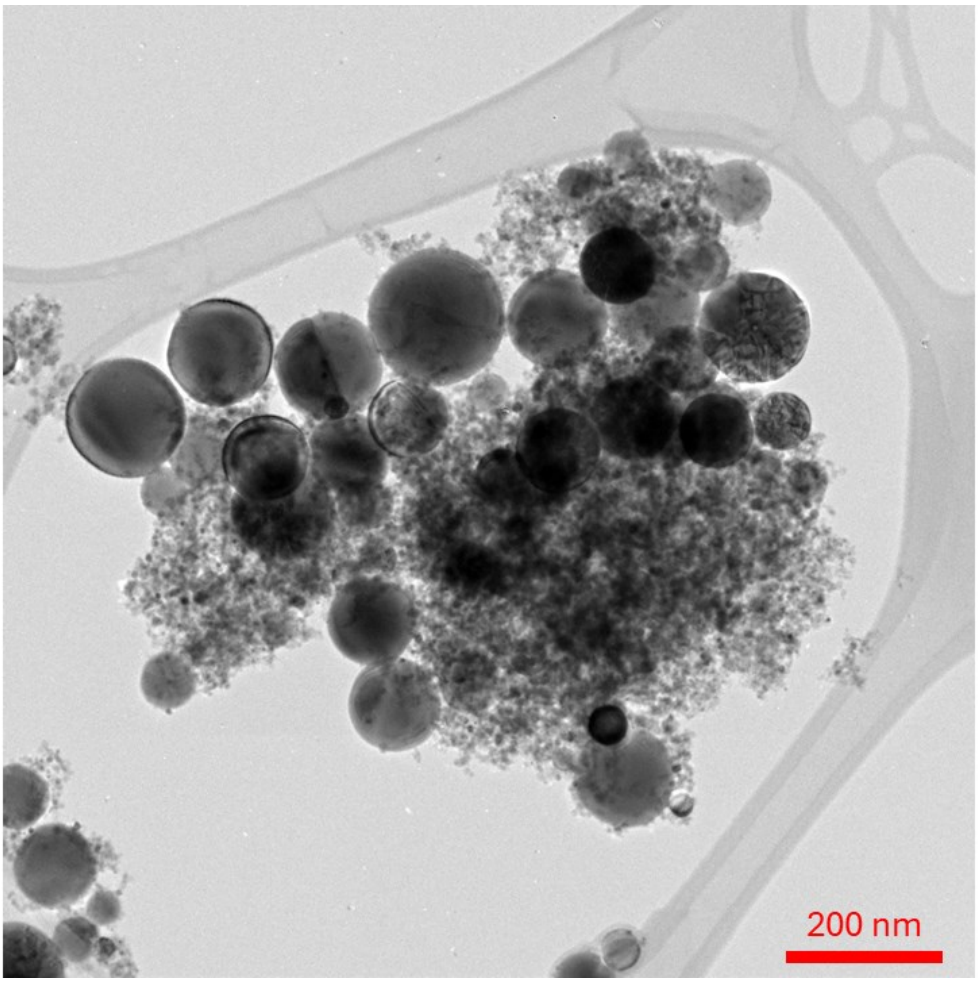

Figure 29: TEM image of heavily agglomerated stainless steel nanoparticles generated from laser ablation in air

5.3.4. Comparison of the main component in the alloy with its respective pure metal

For additional analysis, the recovery of the main component of each alloy was compared to its pure metal counterpart (e.g., copper in brass versus pure copper). This comparison is shown in

Figure 30. From this result, the collection of both copper and aluminum were not strongly affected by the presence of additional alloy components. The most significant difference was the enhanced collection of iron in stainless steel when compared to pure iron.

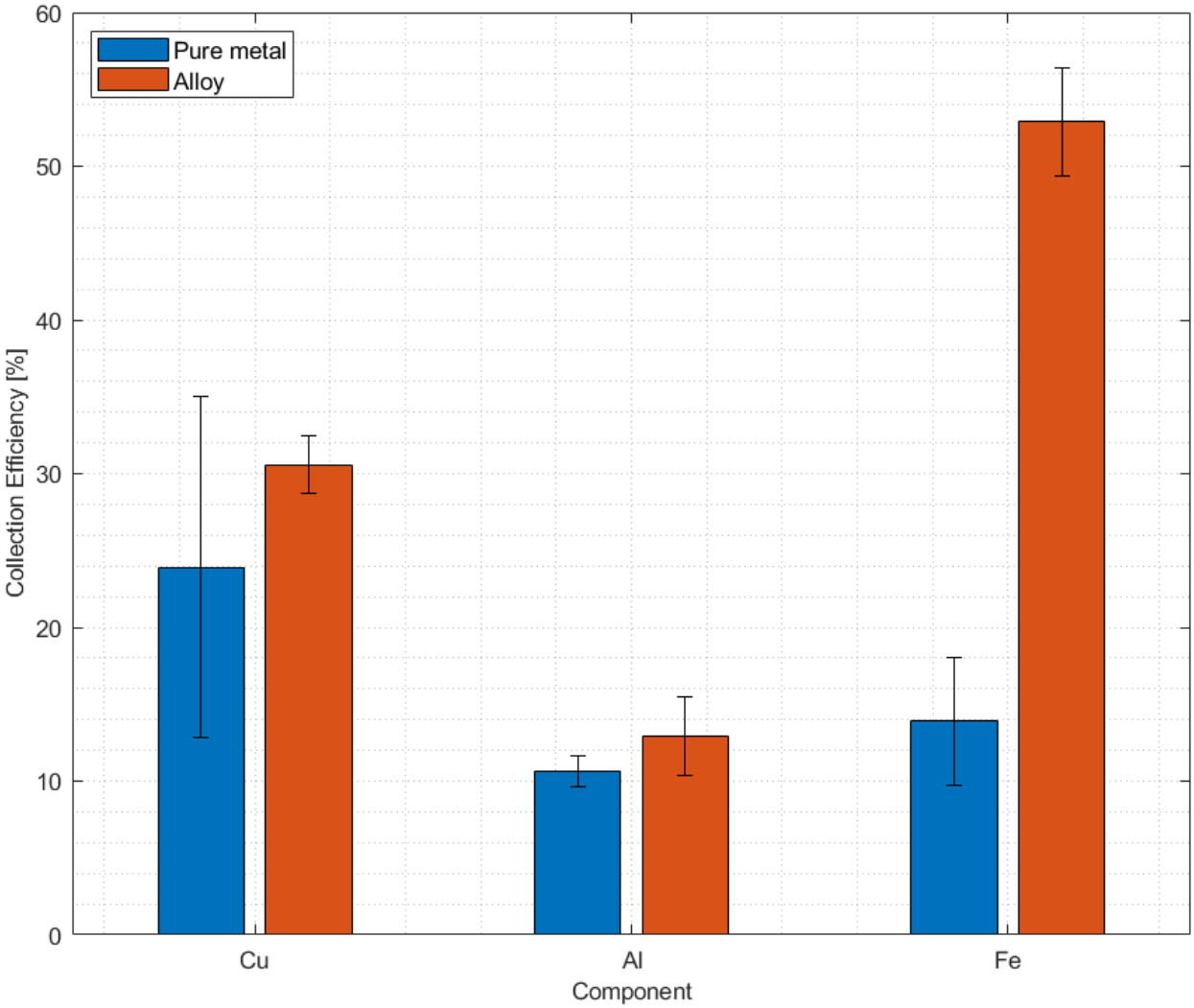

Figure 30: Comparison of main component collection in pure metals versus alloys

To help explain this result, STEM with EDX was used to analyze the nanoparticles generated from pure iron and stainless steel. Figure 31 depicts an iron oxide nanoparticle generated from the pure iron target surrounded by clouds of even smaller iron oxide particles.

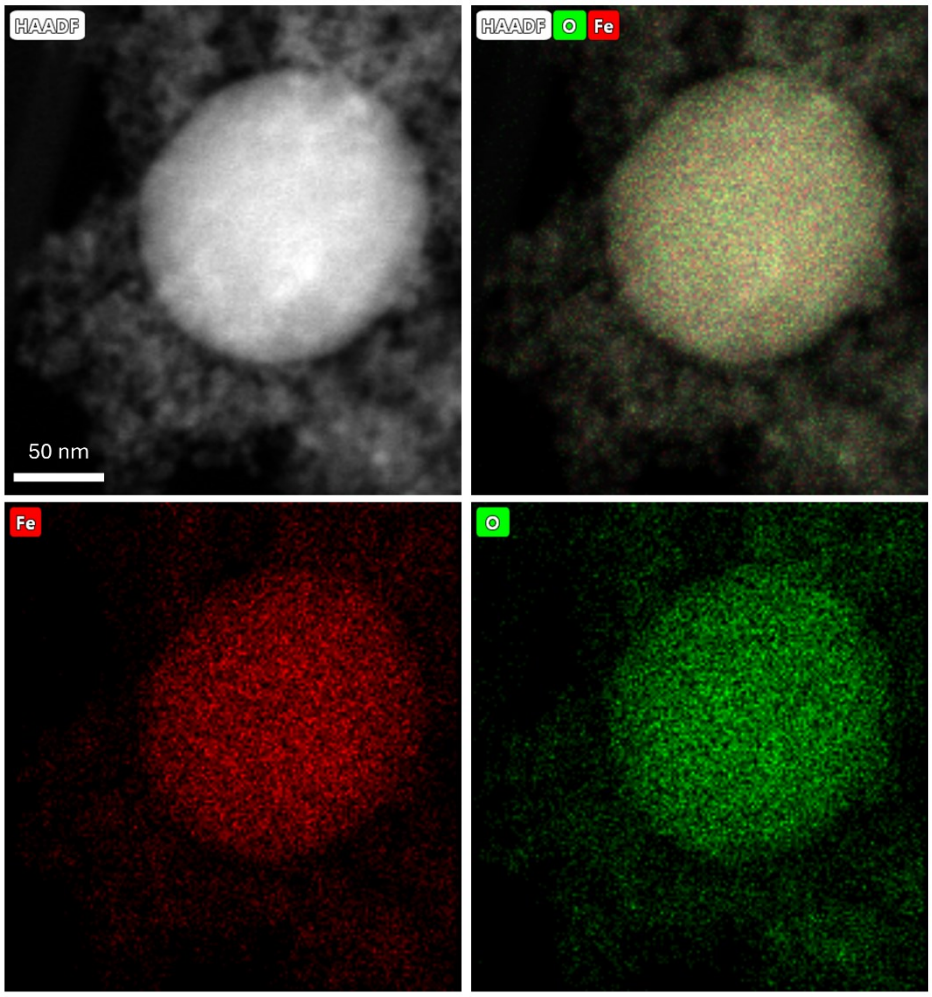

Figure 31: STEM with EDX map of iron oxide nanoparticle

Figure 32 shows stainless steel nanoparticles, providing evidence that multi-element nanoparticles were produced by laser ablation.

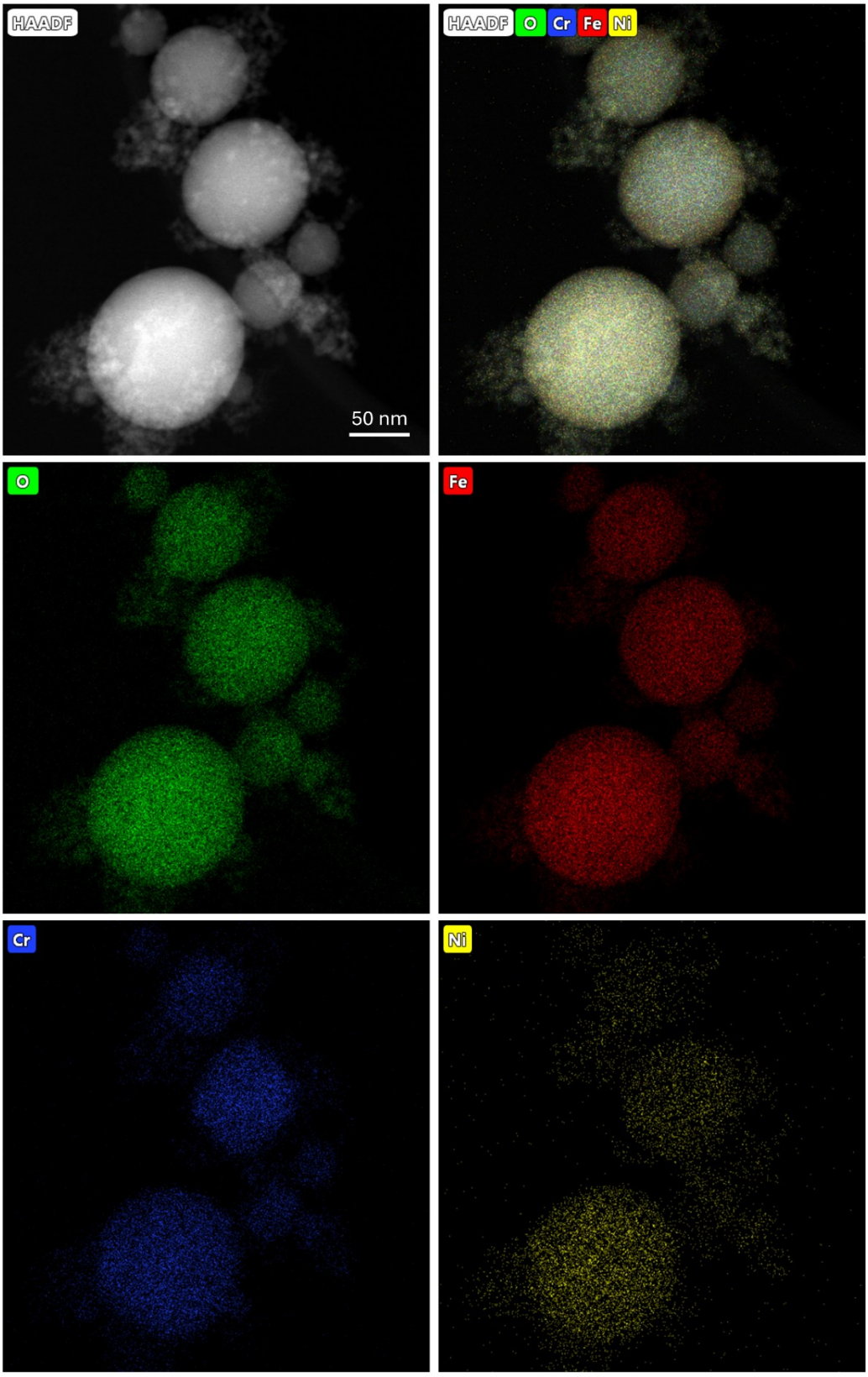

Figure 32: STEM with EDX map of stainless steel nanoparticle

For this alloy, it is evident that the additional components enhanced the collection of iron. One of the key differences between pure iron and stainless steel is how they oxidize in air. It is well known that iron oxidizes readily in the presence of air and moisture. On the other hand, stainless steel does not readily oxidize in air due to its alloying components, particularly chromium. Stainless steel is resistant to oxidation due to the passivation property of chromium [92]. In the presence of air, chromium forms a thin oxide film protecting the underlying metal from further oxidation. In the context of nanoparticle collection, this can have significant ramifications because of the effect of oxygen content on the electrical conductivity of iron containing materials. Compared to pure iron, the electrical conductivity of iron oxide is much lower [93]. Depending on which iron oxide is formed, its electrical conductivity is on the scale of those for semiconductors or insulators [94]. Although stainless steel is not as electrically conductive as pure iron, it is still considered a conductor (unlike iron oxides). Based on the information presented above, it can be concluded that the collection of iron in stainless steel was enhanced due to the oxidation resistant properties of the alloy components, namely chromium. This finding was confirmed by previous work where the removal of silicon ablation debris was directly affected by the amount of silicon oxide formation [95].What could have happened is that the ejected iron nanoparticles oxidized partially (or fully) in their trajectory towards the collector. Similarly, the stainless steel nanoparticles experienced full or partial passivation while being collected. Due to the passivation in stainless steel, the particles experienced a higher electrostatic force towards the collector electrode when compared to the iron oxide. Additionally, once deposited on the electrode, the stainless steel particles also experienced higher electrostatic attraction. Considering the iron oxide collection, the particles were less drawn to the electrode during collection and were less electrostatically attracted to it. This led to losses of iron to the surrounding environment, and from the suction force of the collector setup.

5.4. In-flight functionalization

Unfortunately, the in-flight functionalization trials were not successful for two main reasons:

1. Almost no copper oxide particles were lifted from the powder chamber into the discharge area. Although elevated gas flow rates were used when compared to previous iterations of this work, the already agglomerated copper oxide nanopowder, shown in Figure 33, could not be lifted and moved to the discharge area. Previous iterations of this reactor had both the nanoparticle synthesis and in-flight functionalization in a controlled environment,

therefore, agglomeration was avoided [65, 96]. In this case, since the particles were injected into the reactor, agglomeration was not avoidable.

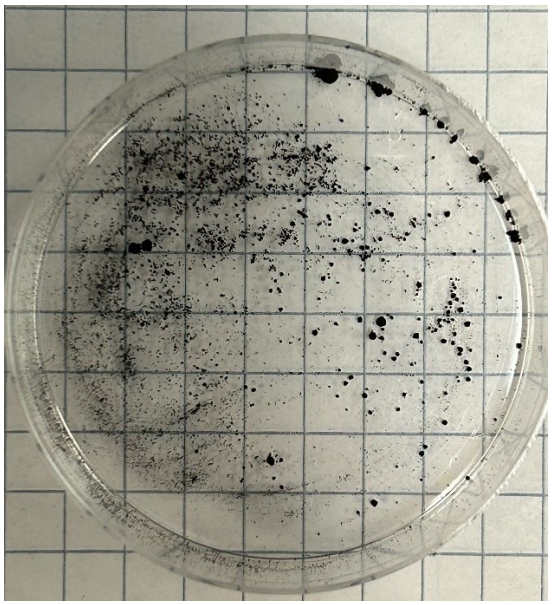

Figure 33: Agglomerated copper oxide nanopowder (the size of a square on the background grid is 6.35 × 6.35 mm^2)

2. For the very low amount of copper oxide powder that did make it to the discharge area, the nanoparticles appeared to be fragmented by the energetic species of the plasma as shown in Figure 34. The particles shown in Figure 34 are comparable in size to what is expected from the specifications of the copper oxide nanopowder. However, they lack the characteristic spherical shape due to deterioration from the plasma. Due to the increased gas flowrate (when compared to previous work), the plasma had a higher density of ions which could have led to bombardment and deterioration of the copper oxide particles [97].

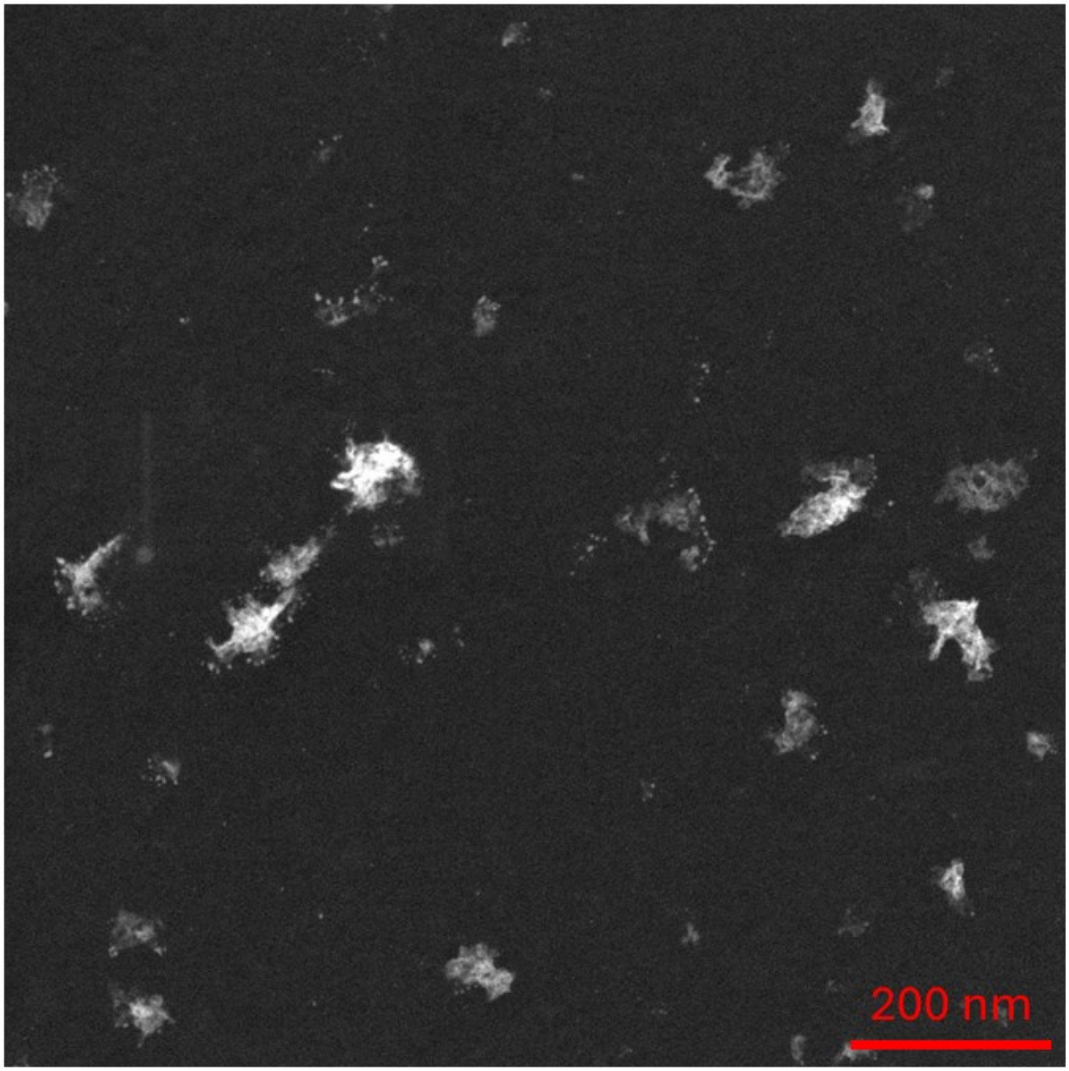

Figure 34: STEM image of copper oxide nanoparticle fragments

Based on these outcomes, it is evident that non-agglomerated particles should be injected into the plasma reactor. This would also allow the reactor to run with lower gas flow rates. In the context of nanoparticle collection, in-flight functionalization as a surface stabilization technique is promising. As highlighted by Figure 29, there certainly is a necessity to surface stabilize particles recovered from laser ablation. Considering laser-machining in a controlled environment, this type of plasma reactor can be implemented downstream from the ablation chamber. In terms of laser ablation in uncontrolled conditions (i.e., in open lab air) several challenges arise for the implementation of the plasma reactor.

The main challenge is maintaining the proper reactor conditions to sustain the plasma discharge. Ideally, one end of the plasma reactor could be placed close to the ablation point so that the nanoparticles can be suctioned into the plasma along with air. However, this is not convenient since at atmospheric pressure, the electric field required to breakdown air is ~30 kV/cm. Therefore, there would need to be significant pressure drop between the initial point of injection of the nanoparticles, and the discharge area of the reactor. The generation of the plasma could be facilitated by the co-injection of argon. Depicted in Figure 35 is a prototype for a suction tube attachment to allow for the injection of argon (to facilitate the plasma generation), and ethane (required for in-flight functionalization).

Figure 35: Tube attachment prototype to facilitate in-flight functionalization in air

Figure 36 shows a cross-section schematic of the protype. The opening on the right side of the attachment would be open to air while the top opening would be sealed to allow for the injection of argon and ethane. Prior to laser machining, a stable plasma can be generated downstream from the attachment. Once the plasma is stable, laser machining can begin during which the nanoparticles could be introduced into the plasma.

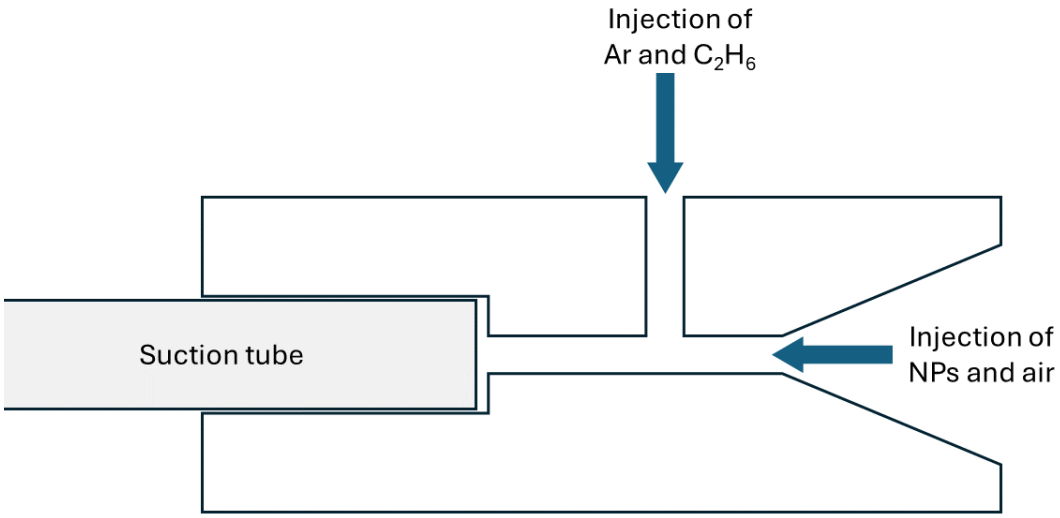

Figure 36: Schematic diagram of tube attachment cross-section

Another factor to consider in implementing the plasma reactor to a laser system is the agglomeration of nanoparticles as they are being produced. It is already well understood that as nanoparticles are ejected, they form agglomerates with each other. Depending on the machining environment, the size distribution of these agglomerates could vary [98]. Therefore, it is possible that in some environments, agglomeration would occur too quickly before individual particles can pass through the reactor. It would also be convenient for the discharge area of the plasma reactor to be as close to the point of ablation as possible. Additionally, depending on the suction rate of the reactor, it is probable that nanoparticles produced using high fluence may eject too quickly for them to be suctioned through the reactor.

6. Conclusions and future work

In this thesis, a novel design for a nanoparticle collector consisting of a rod-shaped electrode and suction line was introduced. Process parameters such as the laser machining stage velocity and suction flow rate were tuned to determine operation settings that optimized nanoparticle collection. It has been determined that machining at a high stage velocity (i.e., low PPS) resulted in optimal collection since there is less interaction between an incoming laser pulse and the expanding ejection plume from a previous pulse. Intermediate suction flow rates led to the best collection since a balance was maintained between attracting the ejected material towards the collector and not executing so much suction that the particles did not accumulate on the electrode. Different laser fluence settings were investigated and it has been shown that for this collector, a lower fluence resulted in more efficient collection. This is caused by the slower material expansion speed for a lower fluence setting causing the ejected particles to take a more direct path towards the collector. Based on this, different designs for nanoparticle collectors can be implemented to consider the effect of fluence dependent dynamics of material ejection. The composition of the target material was studied by comparing the collection of pure metals and alloys. Depending on the alloying elements present, the collection of other metals can be enhanced as was the case for iron in stainless steel 304. Finally, a methodology for in-flight nanoparticle functionalization was tested using a CCRF-DBD plasma reactor. Although initial trials were not successful, this could be a promising technique in the context of collecting and functionalizing particles from laser ablation.

Based on the limitations of the methodology and the conclusions reached in this thesis, future studies to advance this work include:

i. Design and implementation of a nanoparticle collection system for 5-axis laser machining of re-entrant surface structures.

ii. The determination of an optimal collector design or collector settings that take into consideration the fluence dependent dynamics of laser ablated material ejection.

iii. Implementation of the in-flight functionalization plasma reactor to a laser ablation system.

iv. Deeper characterization of the collected nanoparticles, particularly regarding the ablation of alloys.

v. Further investigation of the effect of collection on desired surface structures and redeposited nanoparticles.

vi. Determine the correlation between the dynamics of the plume expansion and the collecting gas dynamics.

7. References

[1] L. Yang, J. Wei, Z. Ma, P. Song, J. Ma, Y. Zhao, Z. Huang, M. Zhang, F. Yang, X. Wang, The Fabrication of Micro/Nano Structures by Laser Machining, Nanomaterials (Basel), 9 (2019) 1789.

[2] G. Pandey, P. Jain, Assessing the nanotechnology on the grounds of costs, benefits, and risks, Beni-Suef University Journal of Basic and Applied Sciences, 9 (2020) 63.

[3] N. Joy, A.-M. Kietzig, In Situ Collection of Nanoparticles during Femtosecond Laser Machining in Air, Nanomaterials, 11 (2021).

[4] B. Suárez-Eiroa, E. Fernández, G. Méndez-Martínez, D. Soto-Oñate, Operational principles of circular economy for sustainable development: Linking theory and practice, Journal of Cleaner Production, 214 (2019) 952-961.

[5] A.Y. Vorobyev, C. Guo, Direct femtosecond laser surface nano/microstructuring and its applications, Laser & Photonics Reviews, 7 (2013) 385-407.

[6] X. Liu, D. Du, G. Mourou, Laser ablation and micromachining with ultrashort laser pulses, IEEE Journal of Quantum Electronics, 33 (1997) 1706-1716.

[7] V. Vercillo, S. Tonnicchia, J.-M. Romano, A. García-Girón, A.I. Aguilar-Morales, S. Alamri, S.S. Dimov, T. Kunze, A.F. Lasagni, E. Bonaccurso, Design Rules for Laser-Treated Icephobic Metallic Surfaces for Aeronautic Applications, Advanced Functional Materials, 30 (2020) 1910268.

[8] F. Sima, K. Sugioka, R.M. Vázquez, R. Osellame, L. Kelemen, P. Ormos, Three-dimensional femtosecond laser processing for lab-on-a-chip applications, Nanophotonics, 7 (2018) 613-634.

[9] L. Wang, Y. Zhao, Y. Yang, X. Pang, L. Hao, Y. Zhao, Piezoresistive 4H-SiC Pressure Sensor With Diaphragm Realized by Femtosecond Laser, IEEE Sensors Journal, 22 (2022) 11535-11542.

[10] C.-H. Hung, F.-Y. Chang, T.-L. Chang, Y.-T. Chang, K.-W. Huang, P.-C. Liang, Micromachining NiTi tubes for use in medical devices by using a femtosecond laser, Optics and Lasers in Engineering, 66 (2015) 34-40.

[11] D.F. Farson, H.W. Choi, B. Zimmerman, J.K. Steach, J.J. Chalmers, S.V. Olesik, L.J. Lee, Femtosecond laser micromachining of dielectric materials for biomedical applications, Journal of Micromechanics and Microengineering, 18 (2008) 035020.

[12] K.M.T. Ahmmed, C. Grambow, A.-M. Kietzig, Fabrication of Micro/Nano Structures on Metals by Femtosecond Laser Micromachining, in: Micromachines, 2014, pp. 1219-1253.

[13] G.L. Eesley, Observation of Nonequilibrium Electron Heating in Copper, Physical Review Letters, 51 (1983) 2140-2143.
[14] S.I. Anisimov, B.L. Kapeliovich, T.L. Perel'Man, Electron emission from metal surfaces exposed to ultrashort laser pulses, Soviet Journal of Experimental and Theoretical Physics, 39 (1974) 375-377.
[15] K.-H. Leitz, B. Redlingshöfer, Y. Reg, A. Otto, M. Schmidt, Metal Ablation with Short and Ultrashort Laser Pulses, Physics Procedia, 12 (2011) 230-238.
[16] E. Gamaly, A. Rode, B. Luther-Davies, Ultrafast Laser Ablation and Film Deposition, in, 2006, pp. 99-129.
[17] S.I. Anisimov, N.A. Inogamov, A.M. Oparin, B. Rethfeld, T. Yabe, M. Ogawa, V.E. Fortov, Pulsed laser evaporation: equation-of-state effects, Applied Physics A, 69 (1999) 617-620.
[18] J. Yang, Y. Zhao, X. Zhu, Theoretical studies of ultrafast ablation of metal targets dominated by phase explosion, Applied Physics A, 89 (2007) 571-578.
[19] N.M. Bulgakova, I.M. Bourakov, Phase explosion under ultrashort pulsed laser ablation: modeling with analysis of metastable state of melt, Applied Surface Science, 197-198 (2002) 41-44.
[20] M. Spellauge, J. Winter, S. Rapp, C. McDonnell, F. Sotier, M. Schmidt, H.P. Huber, Influence of stress confinement, particle shielding and re-deposition on the ultrashort pulse laser ablation of metals revealed by ultrafast time-resolved experiments, Applied Surface Science, 545 (2021) 148930.
[21] C. Wu, L.V. Zhigilei, Microscopic mechanisms of laser spallation and ablation of metal targets from large-scale molecular dynamics simulations, Applied Physics A, 114 (2014) 11-32.
[22] D. Perez, L.J. Lewis, Ablation of Solids under Femtosecond Laser Pulses, Physical Review Letters, 89 (2002) 255504.
[23] J. Yang, Y. Zhao, N. Zhang, Y. Liang, M. Wang, Ablation of metallic targets by high-intensity ultrashort laser pulses, Physical Review B, 76 (2007) 165430.
[24] I.N. Zavestovskaya, A.P. Kanavin, N.A. Men'kova, Crystallization of metals under conditions of superfast cooling when materials are processed with ultrashort laser pulses, J. Opt. Technol., 75 (2008) 353-358.

[25] E.G. Gamaly, N.R. Madsen, M. Duering, A.V. Rode, V.Z. Kolev, B. Luther-Davies, Ablation of metals with picosecond laser pulses: Evidence of long-lived nonequilibrium conditions at the surface, Physical Review B, 71 (2005) 174405.
[26] J. Krüger, W. Kautek, Ultrashort Pulse Laser Interaction with Dielectrics and Polymers, in: T.K. Lippert (Ed.) Polymers and Light, Springer Berlin Heidelberg, Berlin, Heidelberg, 2004, pp. 247-290.
[27] Y. Jee, M.F. Becker, R.M. Walser, Laser-induced damage on single-crystal metal surfaces, J. Opt. Soc. Am. B, 5 (1988) 648-659.
[28] F. Di Niso, C. Gaudiuso, T. Sibillano, F.P. Mezzapesa, A. Ancona, P.M. Lugarà, Influence of the Repetition Rate and Pulse Duration on the Incubation Effect in Multiple-Shots Ultrafast Laser Ablation of Steel, Physics Procedia, 41 (2013) 698-707.
[29] K.M.T. Ahmmed, E.J.Y. Ling, P. Servio, A.-M. Kietzig, Introducing a new optimization tool for femtosecond laser-induced surface texturing on titanium, stainless steel, aluminum and copper, Optics and Lasers in Engineering, 66 (2015) 258-268.
[30] J. Eichstädt, G.R.B.E. Römer, A.J. Huis in ‘t Veld, Determination of irradiation parameters for laser-induced periodic surface structures, Applied Surface Science, 264 (2013) 79-87.
[31] J. Lehr, A.-M. Kietzig, Production of homogenous micro-structures by femtosecond laser micro-machining, Optics and Lasers in Engineering, 57 (2014) 121-129.
[32] N.G. Semaltianos, Nanoparticles by Laser Ablation, Critical Reviews in Solid State and Materials Sciences, 35 (2010) 105-124.
[33] S.A. Irimiciuc, P.-E. Nica, M. Agop, C. Focsa, Target properties – Plasma dynamics relationship in laser ablation of metals: Common trends for fs, ps and ns irradiation regimes, Applied Surface Science, 506 (2020) 144926.
[34] U. Zywietz, C. Reinhardt, A.B. Evlyukhin, T. Birr, B.N. Chichkov, Generation and patterning of Si nanoparticles by femtosecond laser pulses, Applied Physics A, 114 (2014) 45-50.
[35] N. Tsakiris, K.K. Anoop, G. Ausanio, M. Gill-Comeau, R. Bruzzese, S. Amoruso, L.J. Lewis, Ultrashort laser ablation of bulk copper targets: Dynamics and size distribution of the generated nanoparticles, Journal of Applied Physics, 115 (2014) 243301.
[36] A. Menéndez-Manjón, S. Barcikowski, G.A. Shafeev, V.I. Mazhukin, B.N. Chichkov, Influence of beam intensity profile on the aerodynamic particle size distributions generated by femtosecond laser ablation, Laser and Particle Beams, 28 (2010) 45-52.

[37] J. Yin, H. Yan, R. Zhou, Y. Li, A. He, Thermal-Assisted Laser Fabrication of Broadband Ultralow Reflectance Surface by Combining Marangoni Flow with In Situ Deposition, Nanomaterials, 13 (2023) 480.
[38] C.M. Rouleau, C.Y. Shih, C. Wu, L.V. Zhigilei, A.A. Puretzky, D.B. Geohegan, Nanoparticle generation and transport resulting from femtosecond laser ablation of ultrathin metal films: Time-resolved measurements and molecular dynamics simulations, Applied Physics Letters, 104 (2014) 193106.
[39] S. Amoruso, R. Bruzzese, C. Pagano, X. Wang, Features of plasma plume evolution and material removal efficiency during femtosecond laser ablation of nickel in high vacuum, Applied Physics A, 89 (2007) 1017-1024.
[40] S. Amoruso, R. Bruzzese, X. Wang, J. Xia, Propagation of a femtosecond pulsed laser ablation plume into a background atmosphere, Applied Physics Letters, 92 (2008) 041503.
[41] T. Donnelly, G. O'Connell, J.G. Lunney, Metal Nanoparticle Film Deposition by Femtosecond Laser Ablation at Atmospheric Pressure, in: Nanomaterials, 2020.
[42] T. Donnelly, J.G. Lunney, S. Amoruso, R. Bruzzese, X. Wang, X. Ni, Dynamics of the plumes produced by ultrafast laser ablation of metals, Journal of Applied Physics, 108 (2010) 043309.
[43] S.N. Ogugua, O.M. Ntwaeaborwa, H.C. Swart, Latest Development on Pulsed Laser Deposited Thin Films for Advanced Luminescence Applications, in: Coatings, 2020.
[44] J. Lehr, F. de Marchi, L. Matus, J. MacLeod, F. Rosei, A.-M. Kietzig, The influence of the gas environment on morphology and chemical composition of surfaces micro-machined with a femtosecond laser, Applied Surface Science, 320 (2014) 455-465.
[45] J.J. Chang, B.E. Warner, E.P. Dragon, M.W. Martinez, Precision micromachining with pulsed green lasers, Journal of Laser Applications, 10 (1998) 285-291.
[46] X.L. Mao, W.T. Chan, M.A. Shannon, R.E. Russo, Plasma shielding during picosecond laser sampling of solid materials by ablation in He versus Ar atmosphere, Journal of Applied Physics, 74 (1993) 4915-4922.
[47] D. Grojo, J. Hermann, A. Perrone, Plasma analyses during femtosecond laser ablation of Ti, Zr, and Hf, Journal of Applied Physics, 97 (2005) 063306.
[48] A.V. Simakin, V.V. Voronov, N.A. Kirichenko, G.A. Shafeev, Nanoparticles produced by laser ablation of solids in liquid environment, Applied Physics A, 79 (2004) 1127-1132.

[49] E.J. Kautz, D.J. Senor, S.S. Harilal, The interplay between laser focusing conditions, expansion dynamics, ablation mechanisms, and emission intensity in ultrafast laser-produced plasmas, Journal of Applied Physics, 130 (2021).
[50] Z. Zhang, P.A. VanRompay, J.A. Nees, P.P. Pronko, Multi-diagnostic comparison of femtosecond and nanosecond pulsed laser plasmas, Journal of Applied Physics, 92 (2002) 2867-2874.
[51] X. Li, W. Wei, J. Wu, S. Jia, A. Qiu, The Influence of spot size on the expansion dynamics of nanosecond-laser-produced copper plasmas in atmosphere, Journal of Applied Physics, 113 (2013).
[52] G.W. Yang, Laser ablation in liquids: Applications in the synthesis of nanocrystals, Progress in Materials Science, 52 (2007) 648-698.
[53] J.S. Hwang, J.-E. Park, G.W. Kim, H. Nam, S. Yu, J.S. Jeon, S. Kim, H. Lee, M. Yang, Recycling silver nanoparticle debris from laser ablation of silver nanowire in liquid media toward minimum material waste, Scientific Reports, 11 (2021) 2262.
[54] C.M. Rouleau, A.A. Puretzky, D.B. Geohegan, Slowing of femtosecond laser-generated nanoparticles in a background gas, Applied Physics Letters, 105 (2014) 213108.
[55] A.A. Fridman, L.A. Kennedy, Plasma Physics and Engineering, in, CRC Press, Boca Raton, FL, 2011.
[56] Plasma Science and Technology - Basic Fundamentals and Modern Applications, in, InTech.
[57] J.R. Roth, Industrial plasma engineering, Volume 1, Principles, in, CRC Press, [Place of publication not identified], 1995.
[58] U. Kogelschatz, Fundamentals and applications of dielectric-barrier discharges, 1 (2000).
[59] U. Kogelschatz, B. Eliasson, W. Egli, Dielectric-Barrier Discharges. Principle and Applications, Journal de Physique IV Proceedings, 07 (1997) C4-47-C44-66.
[60] K. Ollegott, P. Wirth, C. Oberste-Beulmann, P. Awakowicz, M. Muhler, Fundamental Properties and Applications of Dielectric Barrier Discharges in Plasma-Catalytic Processes at Atmospheric Pressure, Chemie Ingenieur Technik, 92 (2020) 1542-1558.
[61] L. Xu, H.-W. Liang, Y. Yang, S.-H. Yu, Stability and Reactivity: Positive and Negative Aspects for Nanoparticle Processing, Chemical Reviews, 118 (2018) 3209-3250.

[62] O. Baranov, I. Levchenko, J.M. Bell, J.W.M. Lim, S. Huang, L. Xu, B. Wang, D.U.B. Aussems, S. Xu, K. Bazaka, From nanometre to millimetre: a range of capabilities for plasma-enabled surface functionalization and nanostructuring, Materials Horizons, 5 (2018) 765-798.
[63] C. Nessim, M. Boulos, U. Kogelschatz, In-flight coating of nanoparticles in atmospheric-pressure DBD torch plasmas, The European Physical Journal Applied Physics, 47 (2009).
[64] C. Qin, S. Coulombe, Organic layer-coated metal nanoparticles prepared by a combined arc evaporation/condensation and plasma polymerization process, Plasma Sources Science and Technology, 16 (2007) 240.
[65] E.J. Swanson, J. Tavares, S. Coulombe, Improved Dual-Plasma Process for the Synthesis of Coated or Functionalized Metal Nanoparticles, IEEE Transactions on Plasma Science, 36 (2008) 886-887.
[66] P.T. Mannion, J. Magee, E. Coyne, G.M. O'Connor, T.J. Glynn, The effect of damage accumulation behaviour on ablation thresholds and damage morphology in ultrafast laser micro-machining of common metals in air, Applied Surface Science, 233 (2004) 275-287.
[67] J.M. Liu, Simple technique for measurements of pulsed Gaussian-beam spot sizes, Optics Letters, 7 (1982) 196-198.
[68] C.S.R. Nathala, A. Ajami, W. Husinsky, B. Farooq, S.I. Kudryashov, A. Daskalova, I. Bliznakova, A. Assion, Ultrashort laser pulse ablation of copper, silicon and gelatin: effect of the pulse duration on the ablation thresholds and the incubation coefficients, Applied Physics A, 122 (2016) 107.
[69] W. Feng, J. Guo, W. Yan, Y.C. Wan, H. Zheng, Deep channel fabrication on copper by multi-scan underwater laser machining, Optics & Laser Technology, 111 (2019) 653-663.
[70] S.Y. Wang, Y. Ren, C.W. Cheng, J.K. Chen, D.Y. Tzou, Micromachining of copper by femtosecond laser pulses, Applied Surface Science, 265 (2013) 302-308.
[71] L. Hribar, P. Gregorčič, M. Senegačnik, M. Jezeršek, The Influence of the Processing Parameters on the Laser-Ablation of Stainless Steel and Brass during the Engraving by Nanosecond Fiber Laser, Nanomaterials, 12 (2022) 232.
[72] R.R. Behera, M.R. Sankar, P.K. Baruah, A.K. Sharma, A. Khare, Experimental investigations of nanosecond-pulsed Nd:YAG laser beam micromachining on 304 stainless steel, Journal of Micromanufacturing, 1 (2018) 62-75.

[73] M.J. Wood, G. Brock, A.-M. Kietzig, The penguin feather as inspiration for anti-icing surfaces, Cold Regions Science and Technology, 213 (2023) 103903.
[74] K.K. Mandal, A.S. Kuar, S. Mitra, Experimental investigation on laser micro-machining of Al 7075 Alloy, Optics & Laser Technology, 107 (2018) 260-267.
[75] C. Leone, S. Genna, A. Caggiano, V. Tagliaferri, R. Molitierno, An Investigation on Nd:YAG Laser Cutting of Al 6061 T6 Alloy Sheet, Procedia CIRP, 28 (2015) 64-69.
[76] C.G. Novaes, M.A. Bezerra, E.G.P. da Silva, A.M.P.d. Santos, I.L.d.S. Romão, J.H. Santos Neto, A review of multivariate designs applied to the optimization of methods based on inductively coupled plasma optical emission spectrometry (ICP OES), Microchemical Journal, 128 (2016) 331-346.
[77] M.L. Fernández-Sánchez, Atomic Emission Spectrometry | Inductively Coupled Plasma☆, in: P. Worsfold, C. Poole, A. Townshend, M. Miró (Eds.) Encyclopedia of Analytical Science (Third Edition), Academic Press, Oxford, 2019, pp. 169-176.
[78] J. Olesik, ICP-OES capabilities, developments, limitations, and any potential challengers?, Spectroscopy (Santa Monica), 35 (2020) 18-21.
[79] B.V.R. Tata, B. Raj, Confocal laser scanning microscopy: Applications in material science and technology, Bulletin of Materials Science, 21 (1998) 263-278.
[80] S. Wang, I.V. Larina, 8 - High-resolution imaging techniques in tissue engineering, in: R.J. Narayan (Ed.) Monitoring and Evaluation of Biomaterials and their Performance In Vivo, Woodhead Publishing, 2017, pp. 151-180.
[81] W. Zhou, R. Apkarian, Z.L. Wang, D. Joy, Fundamentals of Scanning Electron Microscopy (SEM), in: W. Zhou, Z.L. Wang (Eds.) Scanning Microscopy for Nanotechnology: Techniques and Applications, Springer New York, New York, NY, 2007, pp. 1-40.
[82] S.J. Pennycook, A.R. Lupini, M. Varela, A. Borisevich, Y. Peng, M.P. Oxley, K. Van Benthem, M.F. Chisholm, Scanning Transmission Electron Microscopy for Nanostructure Characterization, in: W. Zhou, Z.L. Wang (Eds.) Scanning Microscopy for Nanotechnology: Techniques and Applications, Springer New York, New York, NY, 2007, pp. 152-191.
[83] Y. Li, X. Zhou, W. Qi, H. Xie, K. Yin, Y. Tong, J. He, S. Gong, Z. Li, Ultrafast fabrication of Cu oxide micro/nano-structures via laser ablation to promote oxygen evolution reaction, Chemical Engineering Journal, 383 (2020) 123086.

[84] J.M.J. Santillán, F.A. Videla, M.B. Fernández van Raap, D.C. Schinca, L.B. Scaffardi, Analysis of the structure, configuration, and sizing of Cu and Cu oxide nanoparticles generated by fs laser ablation of solid target in liquids, Journal of Applied Physics, 113 (2013).
[85] P. Keil, D. Luetzenkirchen-Hecht, R. Frahm, Investigation of Room Temperature Oxidation of Cu in Air by Yoneda-XAFS, AIP Conference Proceedings, 882 (2007) 490-492.
[86] H. Vu, N.-T. Nguyen, N. Kashaninejad, Re-Entrant Microstructures for Robust Liquid Repellent Surfaces, Advanced Materials Technologies, 8 (2023).
[87] S. Paolasini, A. Kietzig, Synchronized videography of plasma plume expansion during femtosecond laser ablation, SPIE, 2014.
[88] T. Ito, Y. Otani, H. Inomata, Performance of air filters cleaned by supercritical carbon dioxide, Separation and Purification Technology, 40 (2004) 41-46.
[89] D.N. Patel, P.K. Pandey, R.K. Thareja, Stoichiometry of laser ablated brass nanoparticles in water and air, Appl. Opt., 52 (2013) 7592-7601.
[90] H. Yahyaoui, B.N. Naoufel, C. Braham, N. Ben Fredj, H. Sidhom, Role of machining defects and residual stress on the AISI 304 fatigue crack nucleation, Fatigue & Fracture of Engineering Materials & Structures, 38 (2014).
[91] A. Moshkovich, V. Perfilyev, I. Lapsker, L. Rapoport, Friction, wear and plastic deformation of Cu and α/β brass under lubrication conditions, Wear, 320 (2014) 34-40.
[92] T. Ohmi, A. Ohki, M. Nakamura, K. Kawada, T. Watanabe, Y. Nakagawa, S. Miyoshi, S. Takahashi, M.S.K. Chen, The Technology of Chromium Oxide Passivation on Stainless Steel Surface, Journal of The Electrochemical Society, 140 (1993) 1691.
[93] D.S. Tannhauser, Conductivity in iron oxides, Journal of Physics and Chemistry of Solids, 23 (1962) 25-34.
[94] V.A. Svetlichnyi, A.V. Shabalina, I.N. Lapin, D.A. Goncharova, D.A. Velikanov, A.E. Sokolov, Study of iron oxide magnetic nanoparticles obtained via pulsed laser ablation of iron in air, Applied Surface Science, 462 (2018) 226-236.
[95] J. Maksimovic, S.H. Ng, T. Katkus, N.H. An Le, J.W.M. Chon, B.C.C. Cowie, T. Yang, Y. Bellouard, S. Juodkazis, Ablation in Externally Applied Electric and Magnetic Fields, Nanomaterials (Basel), 10 (2020).
[96] C. Qin, S. Coulombe, Synthesis of organic layer-coated copper nanoparticles in a dual-plasma process, Materials Letters, 60 (2006) 1973-1976.

[97] D.M. Mattox, Chapter 5 - The Low Pressure Plasma Processing Environment, in: D.M. Mattox (Ed.) Handbook of Physical Vapor Deposition (PVD) Processing (Second Edition), William Andrew Publishing, Boston, 2010, pp. 157-193.
[98] A. Hahn, S. Barcikowski, B. Chichkov, Influences on Nanoparticle Production during Pulsed Laser Ablation, JLMN - Journal of Laser Micro / Nanoengineering, 3 (2008) 73-77.